# Plane strain problem of an elastic matrix containing multiple Gurtin-Murdoch material surfaces along straight segments

Rohit Satish Patil<sup>a</sup>, Sofia G. Mogilevskaya<sup>a,\*</sup>

<sup>a</sup>Department of Civil, Environmental, and Geo-Engineering, University of Minnesota, 500 Pillsbury Drive S.E, 55414, Minneapolis, MN, USA

#### Abstract

This paper presents the study of the plane strain problem of an infinite isotropic elastic medium subjected to far-field load and containing multiple Gurtin-Murdoch material surfaces located along straight segments. Each material segment represents a membrane of vanishing thickness characterized by its own elastic stiffness and residual surface tension. The governing equations, the jump conditions, and the surface tip conditions are reviewed. The displacements in the matrix are sought as the sum of complex variable single-layer elastic potentials whose densities are equal to the jumps in complex tractions across the segments. The densities are found by solving the system of coupled hypersingular boundary integral equations. The approximations by a series of Chebyshev's polynomials of the second kind are used with the square root weight functions chosen to satisfy the tip conditions automatically. Numerical examples are presented to illustrate the influence of dimensionless parameters and to study the effects of interactions.

Keywords: Materials with thin, stiff, and prestressed inhomogeneities /layers, Gurtin-Murdoch model, Hypersingular boundary integral equations, Series of Chebyshev's polynomials

Email address: mogil003@umn.edu (Sofia G. Mogilevskaya)

<sup>\*</sup>Corresponding author.

#### 1. Introduction

In this paper, we consider the plane strain model that can be used to simulate a class of composite materials reinforced with thin, stiff, and prestressed inhomogeneities/layers.

Most of the literature on modeling materials with thin and stiff reinforcements treat them as rigid line inclusions (the so-called stiffeners or anti-cracks). Early papers deal with the problems involving a single straight line rigid inclusion, e.g., [1],[2],[3],[4],[5]. The theoretical and numerical treatments of the problems with multiple rigid straight line inclusions are described in, e.g., [6], [7],[8],[9],[10]; while experimental investigations are reported in, e.g., [11],[12],[13]. Comprehensive reviews of relevant literature can be found in, e.g., [14],[15].

The list of literature related to stiff elastic line inclusions is less extensive. The corresponding boundary value problems include conditions for the fields across the lines of inclusions in terms of the thickness and elastic parameters of original inhomogeneities of finite thicknesses. Those conditions are derived by various types of asymptotic analyses, see, e.g., [16],[17],[18],[19],[20],[21],[22],[23],[24], and the references therein. In those papers, the conditions for both stiff and soft inhomogeneities are derived. The adequate conditions for stiff inhomogeneities include continuity in displacements and jumps in tractions.

Numerical techniques for solving two-dimensional problems with a single or multiple stiff elastic line inclusions in isotropic or anisotropic matrices are reported in several publications, e.g., [25], [26], [27], [28]. In [25] and [27], the problems of multiple elastic line inclusions are solved by using the complex Kolosov-Muskhelishvili potentials and integral representations for the holomorphic functions. In those papers, the line inclusions are arranged in collinear configurations. In [26], the problem of a strip containing a rectilinear arbitrary inclined thin-walled elastic inclusion of finite length is reduced to the system of four singular integral equations and solved using Fourier integral transformation. In [28], the problems of multiple stiff elastic or rigid line inclusions in the multilayered orthotropic medium are studied. The solution technique is based on the use of Fourier transform. The methods used in the above studies are restricted to two-dimensional problems and mostly deal with inclusions located along straight segments. Therefore, those methods cannot be extended for the problems of line inclusions of arbitrary shapes. Additionally, all the above-mentioned publications made an assumption that

inclusions are not prestressed.

In several recent publications, it was proposed to model materials with ultrathin and stiff inhomogeneities using Gurtin-Murdoch [29],[30] and Steigmann-Ogden [31],[32] material surface theories, see [33],[34],[35],[36],[37]. These theories treat the inhomogeneities as either membranes or shells of vanishing thickness characterized by surface elastic parameters and surface tension. The boundary conditions assume continuity of displacements and jumps in tractions across the surfaces. In [34] and [35], it was suggested to use a single-layer elastic potential as a modeling tool, which allows for handling surfaces of arbitrary shapes, both in two and three dimensions. However, the numerical solutions in [33],[34],[35] were obtained for the problems involving a single straight-line inhomogeneity.

Here, we study the problem involving multiple material surfaces located along arbitrarily arranged straight segments inside an infinite isotropic elastic matrix. The theoretical formulation is based on the Gurtin-Murdoch theory, and the single-layer elastic potential tool is used for solving the problem. The paper is organized as follows. Section 2 introduces the problem formulation. In Section 3, we review the governing equations and boundary conditions for the Gurtin-Murdoch model in plane strain setting for the case of material surfaces of arbitrary shapes. The equations and conditions are reformulated in terms of complex variables in Section 4. Section 5 presents the real and complex variable forms of integral representations for the displacements and the complex variable representation for the tractions inside the bulk material, as well as the boundary integral equations for the derivatives of the displacement over the surface. Section 6 focuses on the case of surfaces along straight segments for which it reduces to a system of coupled hypersingular boundary integral equations in terms of the two unknown components of the surface stress tensor. This section also introduces dimensionless variables and the resulting system of coupled dimensionless hypersingular boundary integral equations. The numerical technique for solving the system and for evaluating the elastic fields inside the material system and the stress intensity factors at the tips of the surfaces is described in Section 7, with some details provided in the Appendix A. In Section 8, our model is validated by the comparison with available benchmark solutions. We also present numerical examples showcasing the effects of interactions, the influence of dimensionless surface elasticity and surface tension parameters, as well as far-field loading conditions. Finally, concluding remarks are provided in Section 9.

#### 2. Problem Formulation

Consider the two-dimensional plane strain problem involving an infinite isotropic elastic matrix subjected to uniform far-field stresses  $\sigma^{\infty}$  ( $\sigma_{11}^{\infty}$ ,  $\sigma_{12}^{\infty}$ ,  $\sigma_{22}^{\infty}$ ) and containing N material surfaces  $L = \bigcup_{k=1}^{N} L_k$  each located along the straight segment  $L_k = [a_k, b_k]$ , see Fig. 1. The Gurtin-Murdoch model of material surface is adopted in which a segment represents a vanishing thickness membrane characterized by the shear modulus  $\mu_{\rm S}$ , Lamé parameter  $\lambda_{\rm S}$ , and surface tension  $\sigma_0$ . The elastic properties of the matrix are given by the shear modulus  $\mu$  and Poisson's ratio  $\nu$ . Note that the material surface parameters have dimensions N/m, unlike the elastic parameters of the bulk, whose dimensions are  $N/m^2$ . The goal is to evaluate the elastic fields at any point of the material system and the stress intensity factors at the membranes tips.

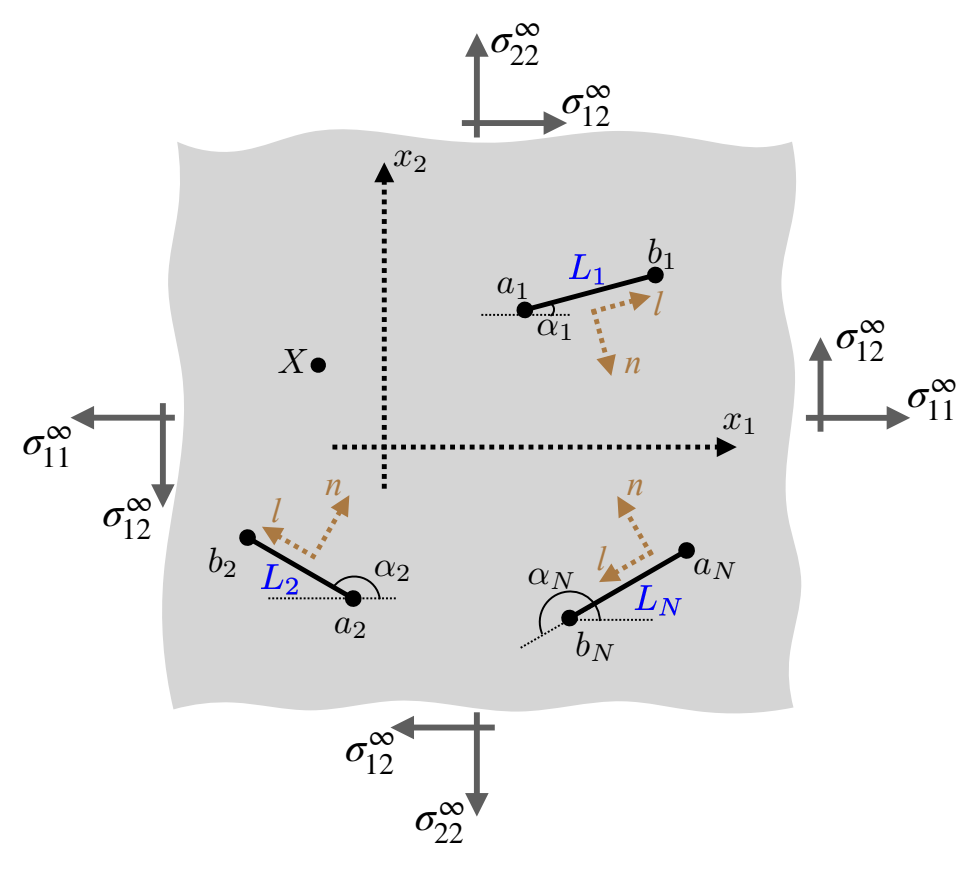


Fig. 1. Problem formulation.

# 3. Review of governing equations of the Gurtin-Murdoch model for the plane strain case

The governing equations for the Gurtin-Murdoch theory are derived in [29],[30] and particularized for the plane strain case in [34], [38]. Here, we review the latter equations for the case of material surface of arbitrary shape. They include the standard Navier equation for the displacements of bulk material and the following supplementary conditions for the elastic fields across and at each material surface (those are valid at any point of the surface):

$$u_1^+ = u_1^- = u_1 ,$$
 $u_2^+ = u_2^- = u_2 ,$ 
(1)

$$\sigma_l^+ - \sigma_l^- = \frac{\partial \sigma^{S}}{\partial s} + \sigma_0 \frac{\omega^{S}}{R} ,$$

$$\sigma_n^+ - \sigma_n^- = -\frac{\sigma^{S}}{R} + \sigma_0 \frac{\partial \omega^{S}}{\partial s} .$$
(2)

The superscripts "+" and "–", used in Eqs. (1)-(2) and throughout the paper, represent the limit values of the corresponding fields as the surface is approached from the direction of the normal vector or from the opposite direction, respectively. The quantities  $u_1$  and  $u_2$  of Eq. (1) denote the components of the displacement vector in the Cartesian coordinates  $(x_1, x_2)$ , while  $\sigma_n$  and  $\sigma_l$  of Eq. (2) represent the normal and shear components of bulk tractions in the local coordinates (n, l), see Fig. 1. Additional quantities involved in Eq. (2) are: the arc length parameter s, the local radius of curvature R = R(s), and the only non-vanishing components  $\sigma^S$  and  $\omega^S$  of the surface stress tensor that are defined as

$$\sigma^{S} = \sigma_{0} + (\lambda_{S} + 2\mu_{S})\varepsilon^{S},$$

$$\omega^{S} = -\frac{u_{l}}{R} + \frac{\partial u_{n}}{\partial s},$$
(3)

in which  $u_n$  and  $u_l$  are the components of displacements in the local coordinates (n, l) and  $\varepsilon^{S}$  is the only nonvanishing component of the surface strain tensor that can be expressed via displacements as

$$\varepsilon^{S} = \frac{u_n}{R} + \frac{\partial u_l}{\partial s} \,. \tag{4}$$

In addition, the following tip conditions must be enforced at the points  $a_k \& b_k$ , k = 1, 2, ...N:

$$\sigma^{S} = 0,$$

$$\sigma_{0}\omega^{S} = 0.$$
(5)

# 4. Complex variables form of the equations

As demonstrated in [34] and [38], it is beneficial to reformulate Eqs. (1)-(4) using the formalism of complex variables as

$$u^+ = u^- \,, \tag{6a}$$

$$\Delta \sigma = \sigma^{+} - \sigma^{-} = -\frac{\widetilde{R}}{R} \left[ \frac{\sigma_{0}}{\widetilde{R}} + 2\eta_{1}u' + 2\eta_{2}\overline{u'} \right]$$

$$+2i\widetilde{R} [\eta_{1}u'' \exp(i\alpha) + \eta_{2}\overline{u''} \exp(-i\alpha)],$$
(6b)

$$\sigma^{S} = \sigma_0 + (2\mu_S + \lambda_S) \operatorname{Re}(u') , \qquad (6c)$$

$$\omega^{S} = -Im(u'), \qquad (6d)$$

where  $u = u_1 + \mathrm{i} u_2$ ,  $\sigma = \sigma_n + \mathrm{i} \sigma_l$ ,  $\mathrm{i}^2 = -1$ ,  $\alpha$  is the angle between the axis  $Ox_1$  and the tangent at the point where the traction jumps are evaluated,  $\widetilde{R}$  is a characteristic geometric parameter, such as, e.g., the average radius of surface curvature, and the bar above the symbol indicates complex conjugation. The notation u' is used to identify the first derivative of the complex displacement u on the surface, e.g.

$$u' = \frac{\partial u}{\partial z} + \frac{\partial u}{\partial \overline{z}} \frac{\mathrm{d}\overline{z}}{\mathrm{d}z} \,, \tag{7}$$

and the second derivative, u'' is defined in a similar manner.

Additional notations used in Eq. (6) are

$$\eta_{1} = \frac{2\mu_{S} + \lambda_{S} + \sigma_{0}}{4\widetilde{R}} ,$$

$$\eta_{2} = \frac{2\mu_{S} + \lambda_{S} - \sigma_{0}}{4\widetilde{R}} .$$
(8)

### 5. Governing integral representations

If the displacements in the matrix are expressed in the form of a single layer elastic potential, [39], the conditions of continuity of the displacements and jumps in tractions are automatically fulfilled, as explained in [40],[41]. In real variables, the corresponding expression for each displacement component has the following form:

$$u_k(\mathbf{x}) = u_k^{\infty}(\mathbf{x}) + \int_L \Delta t_j(\boldsymbol{\zeta}) G_{kj}(\mathbf{x}, \boldsymbol{\zeta}) ds_{\zeta} \; ; \; k, j = 1, 2 \; , \tag{9}$$

where L is the totality of the material surfaces,  $u_k^{\infty}(\mathbf{x})$  is the corresponding component of the displacements in the homogeneous plane (without material surfaces) due to the far-field load,  $\Delta t_j(\zeta) = t_j^+(\zeta) - t_j^-(\zeta)$  are the components of jumps in tractions across the surfaces in the Cartesian coordinate system, and the repeated index implies summation. The kernel  $G_{kj}(\mathbf{x}, \zeta)$  of Eq. (9) is the following Kelvin fundamental solution:

$$G_{kj}(\mathbf{x}, \boldsymbol{\zeta}) = \frac{1}{2\pi\mu(\kappa+1)} [-\kappa \delta_{kj} \ln r + r_{,k} r_{,j}], \qquad (10)$$

in which  $\delta_{kj}$  is Kronecker's symbol,  $\kappa = 3 - 4\nu$ ,  $r = |\mathbf{x} - \boldsymbol{\zeta}|$ ,  $r_k = x_k - \zeta_k$ ,  $r_{,k} = \partial r/\partial x_k$ .

The complex variables form of the above representations were obtained in [41], [42], [43]. The integral representation for the complex displacements outside of L can be expressed as follows:

$$u(z) = u^{\infty}(z) - \frac{1}{4\pi i \mu(\kappa + 1)} \left\{ \int_{L} \Delta \sigma(\tau) [2\kappa \ln(z - \tau) - \kappa K_{1}(\tau, z)] d\tau + \int_{L} \overline{\Delta \sigma(\tau)} K_{2}(\tau, z) d\overline{\tau} \right\},$$
(11)

in which  $z = x_1 + ix_2 \notin L$ ,

$$K_1(\tau, z) = \ln\left(\frac{\tau - z}{\overline{\tau} - \overline{z}}\right) ,$$

$$K_2(\tau, z) = \left(\frac{\tau - z}{\overline{\tau} - \overline{z}}\right) ,$$
(12)

and

$$u^{\infty}(z) = \frac{1}{2\mu} \left[ (\kappa - 1) \frac{\sigma_{11}^{\infty} + \sigma_{22}^{\infty}}{4} z - \frac{\sigma_{22}^{\infty} - \sigma_{11}^{\infty} - 2i\sigma_{12}^{\infty}}{2} \overline{z} \right] . \tag{13}$$

The complex tractions on some line outside of L can be represented by the following integral expression:

$$\sigma(z) = \sigma^{\infty}(z) - \frac{1}{2\pi i(\kappa + 1)} \left\{ \int_{L} \Delta \sigma(\tau) \left[ \frac{(\kappa - 1)}{\tau - z} + \kappa \frac{\partial K_{1}(\tau, z)}{\partial z} \right] d\tau - \int_{L} \overline{\Delta \sigma(\tau)} \frac{\partial K_{2}(\tau, z)}{\partial z} d\tau \right\}, \quad (14)$$

where

$$\sigma^{\infty}(z) = \frac{\sigma_{11}^{\infty} + \sigma_{22}^{\infty}}{2} + \frac{\sigma_{22}^{\infty} - \sigma_{11}^{\infty} - 2i\sigma_{12}^{\infty}}{2} \frac{\mathrm{d}\overline{z}}{\mathrm{d}z}.$$
 (15)

Using Eq. (11), one can obtain the following equation (in which the derivatives are defined as in Eq. (7)):

$$u'(z) = [u^{\infty}(z)]' - \frac{1}{4\pi i \mu(\kappa + 1)} \left\{ \int_{L} \Delta \sigma(\tau) \left[ 2\kappa \frac{1}{z - \tau} - \kappa \frac{\partial K_{1}(\tau, z)}{\partial z} \right] d\tau + \int_{L} \overline{\Delta \sigma(\tau)} \frac{\partial K_{2}(\tau, z)}{\partial z} d\overline{\tau} \right\}, \quad (16)$$

where

$$[u^{\infty}(z)]' = \frac{1}{2\mu} \left[ (\kappa - 1) \frac{\sigma_{11}^{\infty} + \sigma_{22}^{\infty}}{4} - \frac{\sigma_{22}^{\infty} - \sigma_{11}^{\infty} - 2i\sigma_{12}^{\infty}}{2} \frac{d\overline{z}}{dz} \right] . \tag{17}$$

It has been proved in [34] that u'(z) is continuous when  $z \to \tau^0 = \tau_1^0 + i\tau_2^0 \in L$ , thus the resulting boundary integral equation on L is

$$\lim_{z \to \pm \tau^{0}} u'(z) = u'(\tau^{0}) = [u^{\infty}(\tau^{0})]'$$

$$- \frac{1}{4\pi i \mu(\kappa + 1)} \left\{ \int_{L} \Delta \sigma(\tau) \left[ \frac{2\kappa}{\tau^{0} - \tau} - \kappa \frac{\partial K_{1}(\tau, \tau^{0})}{\partial \tau^{0}} \right] d\tau + \int_{L} \overline{\Delta \sigma(\tau)} \frac{\partial K_{2}(\tau, \tau^{0})}{\partial \tau^{0}} d\overline{\tau} \right\}, \quad (18)$$

where the symbol f identifies the principal value of Cauchy types integral.

### 6. The particularization for the case of straight segments

The equations reviewed in Sections 3-5 were for the case of arbitrarily curved surfaces. Here, we particularize them for the case under study in which the surfaces are located along straight segments. In such case, 1/R = 0 and angle  $\alpha$  is constant along each segment but can be different for different segments. Thus, Eq. (2) reduces to

$$\sigma_l^+ - \sigma_l^- = \frac{\partial \sigma^{S}}{\partial s} ,$$

$$\sigma_n^+ - \sigma_n^- = \sigma_0 \frac{\partial \omega^{S}}{\partial s} ,$$
(19)

and the expression for the jumps in complex tractions across each segment can be recast as

$$\Delta \sigma = \sigma_0 \frac{\partial \omega^{S}}{\partial s} + i \frac{\partial \sigma^{S}}{\partial s} . \tag{20}$$

Taking into account that  $d\tau = \exp(i\alpha) ds$ , Eqs. (19)-(20) can be rewritten as follows (the arguments were omitted for brevity):

$$\sigma_l^+ - \sigma_l^- = \exp(i\alpha) \frac{\partial \sigma^S}{\partial \tau} ,$$

$$\sigma_n^+ - \sigma_n^- = \sigma_0 \exp(i\alpha) \frac{\partial \omega^S}{\partial \tau} ,$$

$$\Delta \sigma = \left(\sigma_0 \frac{\partial \omega^S}{\partial \tau} + i \frac{\partial \sigma^S}{\partial \tau}\right) \exp(i\alpha) .$$
(21)

From Eq. (18) we obtain the following system of equations for  $\tau^0 \in L_k$ , k = 1, 2, ...N for our case:

$$u'(\tau^{0}) = [u^{\infty}(\tau^{0})]'$$

$$+ \frac{1}{4\pi i \mu(\kappa + 1)} \left\{ \int_{L_{k}} \Delta \sigma(\tau) \left( \frac{2\kappa}{\tau - \tau^{0}} \right) d\tau \right.$$

$$+ \sum_{p=1, p \neq k}^{N} \left[ \int_{L_{p}} \Delta \sigma(\tau) \left[ \frac{2\kappa}{\tau^{0} - \tau} - \kappa \frac{\partial K_{1}(\tau, \tau^{0})}{\partial \tau^{0}} \right] d\tau + \int_{L_{p}} \overline{\Delta \sigma(\tau)} \frac{\partial K_{2}(\tau, \tau^{0})}{\partial \tau^{0}} d\overline{\tau} \right] \right\},$$

$$(22)$$

where

$$\frac{\partial K_1(\tau, \tau^0)}{\partial \tau^0} = \begin{cases}
0 & \text{if } \tau^0, \tau \in L_k \\
\frac{\exp(-2i\alpha_k)}{\overline{\tau} - \overline{\tau}^0} - \frac{1}{(\tau - \tau^0)} & \text{if } \tau^0 \in L_k, \tau \notin L_k
\end{cases}$$

$$\frac{\partial K_2(\tau, \tau^0)}{\partial \tau^0} = \begin{cases}
0 & \text{if } \tau^0, \tau \in L_k \\
\frac{(\tau - \tau^0) \exp(-2i\alpha_k) - (\overline{\tau} - \overline{\tau}^0)}{(\overline{\tau} - \overline{\tau}^0)^2} & \text{if } \tau^0 \in L_k, \tau \notin L_k
\end{cases}$$
(23)

in which the angles  $\alpha_k$  are shown on Fig.1.

With the use of Eqs. (6(c)-(d)), system of Eq. (22) can be rewritten as the system of 2N coupled hypersingular boundary integral equations in terms of  $\sigma^{S}$  and  $\omega^{S}$ . The resulting expressions are rather long and not presented here.

#### 6.1. Integral equations in dimensionless form

Introducing the following dimensionless variables:

$$\widetilde{\sigma} = \sigma_n/\mu + i \,\sigma_l/\mu \,,$$

$$\widetilde{\sigma}_{ij} = \sigma_{ij}/\mu \,,$$

$$\widetilde{\sigma}^{S}|_{L_k} = \sigma^{S}(\tau)/\mu l_k \,; \, \tau \in L_k \,,$$

$$\widetilde{\sigma}_{0}|_{L_k} = \sigma_{0}(\tau)/\mu l_k \,; \, \tau \in L_k \,,$$

$$\gamma_k = \frac{2\mu l_k}{2\mu_S + \lambda_S} \,,$$

$$\widetilde{u} = (u_1/a) + i \,(u_2/a) \,,$$
(24)

where  $l_k$  is the half-length of the  $L_k$ , and a is the characteristic length, e.g., the arithmetic average of all  $l_k$ , k = 1, 2, ...N. One can also rewrite  $\tau \in L_k$  as  $Zc_k + l_k \exp(i\alpha_k) \tilde{\tau}$  with  $Zc_k = (a_k + b_k)/2$  and  $-1 \leq \tilde{\tau} \leq 1$ .

With those notations, the coupled system of 2N dimensionless hypersingular boundary integral equations has the following form (k = 1, 2, ..., N):

$$\gamma_{k} \widetilde{\sigma}^{S}|_{L_{k}} = \gamma_{k} \widetilde{\sigma}_{0}|_{L_{k}} + \widetilde{\Sigma_{1}^{k}} + \frac{\kappa}{\pi (\kappa + 1)} \oint_{-1}^{1} \widetilde{\sigma}^{S}|_{L_{k}} \frac{d\widetilde{\tau}}{(\widetilde{\tau} - \widetilde{\tau}^{0})^{2}} \\
+ \frac{1}{\pi (\kappa + 1)} \sum_{p=1, p \neq k}^{N} Re \left\{ \overline{C_{1p}^{(\sigma_{k})}} \int_{-1}^{1} \widetilde{\sigma}^{S}|_{L_{p}} \frac{d\widetilde{\tau}}{(\widetilde{\tau} + \widehat{Z_{pk}})^{2}} + \overline{C_{2p}^{(\sigma_{k})}} \int_{-1}^{1} \widetilde{\sigma}^{S}|_{L_{p}} \frac{d\widetilde{\tau}}{(\widetilde{\tau} + \widehat{Z_{pk}})^{3}} \right. \\
+ \overline{C_{3p}^{(\sigma_{k})}} \int_{-1}^{1} \omega^{S}|_{L_{p}} \frac{d\widetilde{\tau}}{(\widetilde{\tau} + \widehat{Z_{pk}})^{2}} + \overline{C_{4p}^{(\sigma_{k})}} \int_{-1}^{1} \omega^{S}|_{L_{p}} \frac{d\widetilde{\tau}}{(\widetilde{\tau} + \widehat{Z_{pk}})^{3}} \right\}, (25)$$

$$\omega^{S}|_{L_{k}} = -\widetilde{\Sigma}_{2}^{k} + \frac{\widetilde{\sigma}_{0}|_{L_{k}} \kappa}{2\pi(\kappa + 1)} \oint_{-1}^{1} \omega^{S}|_{L_{k}} \frac{d\widetilde{\tau}}{(\widetilde{\tau} - \widetilde{\tau}^{0})^{2}} 
+ \frac{1}{2\pi(\kappa + 1)} \sum_{p=1, p\neq k}^{N} Re \left\{ \overline{C_{1p}^{(\omega_{k})}} \int_{-1}^{1} \widetilde{\sigma}^{S}|_{L_{p}} \frac{d\widetilde{\tau}}{(\widetilde{\tau} + \widehat{Z_{pk}})^{2}} + \overline{C_{2p}^{(\omega_{k})}} \int_{-1}^{1} \widetilde{\sigma}^{S}|_{L_{p}} \frac{d\widetilde{\tau}}{(\widetilde{\tau} + \widehat{Z_{pk}})^{3}} \right. 
\left. + \overline{C_{3p}^{(\omega_{k})}} \int_{-1}^{1} \omega^{S}|_{L_{p}} \frac{d\widetilde{\tau}}{(\widetilde{\tau} + \widehat{Z_{pk}})^{2}} + \overline{C_{4p}^{(\omega_{k})}} \int_{-1}^{1} \omega^{S}|_{L_{p}} \frac{d\widetilde{\tau}}{(\widetilde{\tau} + \widehat{Z_{pk}})^{3}} \right\}, (26)$$

where the symbol  $\neq$  denotes the Hadamard finite part integral, and

$$\widetilde{\Sigma}_{1}^{k} = \frac{(\kappa - 1) + 2\cos(2\alpha_{k})}{4} \,\widetilde{\sigma}_{11}^{\infty} + \frac{(\kappa - 1) - 2\cos(2\alpha_{k})}{4} \,\widetilde{\sigma}_{22}^{\infty} + \sin(2\alpha_{k}) \,\widetilde{\sigma}_{12}^{\infty} ,$$

$$\widetilde{\Sigma}_{2}^{k} = \frac{\sin(2\alpha_{k})}{2} \left( \,\widetilde{\sigma}_{22}^{\infty} - \,\widetilde{\sigma}_{11}^{\infty} \right) + \frac{\cos(2\alpha_{k})}{2} \,\widetilde{\sigma}_{12}^{\infty} ,$$

$$\widehat{\mathcal{Z}_{pk}} = \left( \frac{Zc_{p} - z}{l_{p}} \right) \exp\left(-\mathrm{i}\alpha_{p}\right) \dots z \in L_{k} .$$
(27)

The complex constants for Eqs. (25)-(26) are given by:

• Constants for Eq. (25)

$$C_{1p}^{(\sigma_k)} = \frac{1}{2} \left[ (1+\kappa) \exp\left(2i(\alpha_p - \alpha_k)\right) - (1-\kappa) \right] ,$$

$$C_{2p}^{(\sigma_k)} = 2i \operatorname{Im}(\widehat{\mathcal{Z}}_{pk}) \exp\left(2i(\alpha_p - \alpha_k)\right) ,$$

$$C_{3p}^{(\sigma_k)} = \frac{\widetilde{\sigma}_0|_{L_p}}{2i} (1-\kappa) \left[ 1 - \exp\left(2i(\alpha_p - \alpha_k)\right) \right] ,$$

$$C_{4p}^{(\sigma_k)} = -2 \left(\widetilde{\sigma}_0|_{L_p}\right) \operatorname{Im}(\widehat{\mathcal{Z}}_{pk}) \exp\left(2i(\alpha_p - \alpha_k)\right) .$$

$$(28)$$

• Constants for Eq. (26)

$$C_{1p}^{(\omega_k)} = \frac{1}{2i} (1 + \kappa) \left[ 1 - \exp\left(2i(\alpha_p - \alpha_k)\right) \right] ,$$

$$C_{2p}^{(\omega_k)} = -2 \operatorname{Im}(\widehat{\mathcal{Z}}_{pk}) \exp\left(2i(\alpha_p - \alpha_k)\right) ,$$

$$C_{3p}^{(\omega_k)} = \frac{\widetilde{\sigma}_0|_{L_p}}{2} \left[ (1 + \kappa) - (1 - \kappa) \exp\left(2i(\alpha_p - \alpha_k)\right) \right] ,$$

$$C_{4p}^{(\omega_k)} = -2i \left(\widetilde{\sigma}_0|_{L_p}\right) \exp\left(2i(\alpha_p - \alpha_k)\right) .$$

$$(29)$$

#### 7. Numerical solution technique

# 7.1. Approximations

As in [34], we will use the following approximations for  $\tilde{\sigma}^{S}$  and  $\omega^{S}$ :

$$\widetilde{\sigma}^{\mathrm{S}}|_{L_k} = \sqrt{1 - (\widetilde{\tau})^2} \sum_{m=0}^n (A_k)_m U_m(\widetilde{\tau}) \dots \tau \in L_k ,$$
 (30)

$$\omega^{S}|_{L_{k}} = \sqrt{1 - (\widetilde{\tau})^{2}} \sum_{m=0}^{n} (B_{k})_{m} U_{m}(\widetilde{\tau}) \dots \widetilde{\tau} \in L_{k},$$
(31)

where  $U_m(\tilde{\tau})$  is the Chebyshev polynomial of second kind of degree m,  $(A_k)_m$ ,  $(B_k)_m$  are the unknown coefficients for the k-th segment, and n is the maximum degree of the approximation, which we assume to be the same for all segments. The square root weight function is used in order to automatically satisfy the tip conditions, i.e.,  $\tilde{\sigma}^S = 0$ ,  $\tilde{\sigma}_0 \omega^S = 0$ .

### 7.2. System of linear algebraic equations

Substituting approximations of Eqs. (30)-(31), into hypersingular equations Eqs. (25)-(26), multiplying them by  $U_j(\tilde{\tau})$ ,  $j = \{0, 1, ..., n\}$ , and using orthogonality properties of Chebyshev polynomials, we obtain the following systems of linear algebraic equations with respect to the unknown coefficients  $(A_k)_m$ ,  $(B_k)_m$ ,  $k = \{1, 2, ..., N\}$ :

$$\sum_{m=0}^{n} (\Phi_{k})_{jm} (A_{k})_{m} - \frac{1}{\pi(1+\kappa)} \left\{ \sum_{p=1, p \neq k}^{N} \left[ \sum_{m=0}^{n} (\phi_{p})_{jm} (A_{p})_{m} + \sum_{m=0}^{n} (\varphi_{p})_{jm} (B_{p})_{m} \right] \right\} \\
= \left( \gamma_{k} (\widetilde{\sigma_{0}})_{k} + \widetilde{\Sigma_{1}^{k}} \right) \left( \frac{1 + (-1)^{j}}{1+j} \right) ; j = \{0, 1, 2, ...n\} , \quad (32)$$

$$\sum_{m=0}^{n} (\Psi_k)_{jm} (B_k)_m - \frac{1}{2\pi(1+\kappa)} \left\{ \sum_{p=1, p\neq k}^{N} \left[ \sum_{m=0}^{n} (\chi_p)_{jm} (A_p)_m + \sum_{m=0}^{n} (\psi_p)_{jm} (B_p)_m \right] \right\} \\
= -\widetilde{\Sigma}_2^k \left( \frac{1 + (-1)^j}{j+1} \right) ; j = \{0, 1, 2, ...n\} , \quad (33)$$

where,

$$(\Phi_k)_{jm} = \frac{\pi}{2} \gamma_k \delta_{jm} + \frac{k}{1+k} (m+1) \int_{-1}^1 U_m(\widetilde{\tau}) U_j(\widetilde{\tau}) d\widetilde{\tau} ,$$

$$(\Psi_k)_{mj} = \frac{\pi}{2} \delta_{jm} + \frac{(\widetilde{\sigma}_0)_k k}{2(1+k)} (m+1) \int_{-1}^1 U_m(\widetilde{\tau}) U_j(\widetilde{\tau}) d\widetilde{\tau} ,$$
(34)

$$(\phi_p)_{jm} = \int_{-1}^1 Re \left\{ \overline{C_{1p}^{(\sigma_k)}} \int_{-1}^1 U_m(\widetilde{\tau}) \frac{\sqrt{1 - (\widetilde{\tau})^2}}{(\widetilde{\tau} + \widehat{Z_{pk}})^2} d\widetilde{\tau} + \overline{C_{2p}^{(\sigma_k)}} \int_{-1}^1 U_m(\widetilde{\tau}) \frac{\sqrt{1 - (\widetilde{\tau})^2}}{(\widetilde{\tau} + \widehat{Z_{pk}})^3} d\widetilde{\tau} \right\} U_j(\widetilde{\tau}) d\widetilde{\tau} , \quad (35)$$

$$(\varphi_p)_{jm} = \int_{-1}^{1} Re \left\{ \overline{C_{3p}^{(\sigma_k)}} \int_{-1}^{1} U_m(\widetilde{\tau}) \frac{\sqrt{1 - (\widetilde{\tau})^2}}{(\widetilde{\tau} + \widehat{Z_{pk}})^2} d\widetilde{\tau} + \overline{C_{4p}^{(\sigma_k)}} \int_{-1}^{1} U_m(\widetilde{\tau}) \frac{\sqrt{1 - (\widetilde{\tau})^2}}{(\widetilde{\tau} + \widehat{Z_{pk}})^3} d\widetilde{\tau} \right\} U_j(\widetilde{\tau}) d\widetilde{\tau} , \quad (36)$$

$$(\chi_p)_{jm} = \int_{-1}^1 Re \left\{ \overline{C_{1p}^{(\omega_k)}} \int_{-1}^1 U_m(\widetilde{\tau}) \frac{\sqrt{1 - (\widetilde{\tau})^2}}{(\widetilde{\tau} + \widehat{Z_{pk}})^2} d\widetilde{\tau} + \overline{C_{2p}^{(\omega_k)}} \int_{-1}^1 U_m(\widetilde{\tau}) \frac{\sqrt{1 - (\widetilde{\tau})^2}}{(\widetilde{\tau} + \widehat{Z_{pk}})^3} d\widetilde{\tau} \right\} U_j(\widetilde{\tau}) d\widetilde{\tau} , \quad (37)$$

$$(\psi_p)_{jm} = \int_{-1}^1 Re \left\{ \overline{C_{3p}^{(\omega_k)}} \int_{-1}^1 U_m(\widetilde{\tau}) \frac{\sqrt{1 - (\widetilde{\tau})^2}}{(\widetilde{\tau} + \widehat{Z_{pk}})^2} d\widetilde{\tau} + \overline{C_{4p}^{(\omega_k)}} \int_{-1}^1 U_m(\widetilde{\tau}) \frac{\sqrt{1 - (\widetilde{\tau})^2}}{(\widetilde{\tau} + \widehat{Z_{pk}})^3} d\widetilde{\tau} \right\} U_j(\widetilde{\tau}) d\widetilde{\tau} . \quad (38)$$

### 7.3. Evaluation of integrals

The system described in Section 7.2 involves several types of integrals. The non-singular integral of Eq. (34) was computed using the built-in numerical integration function 'integral' in MATLAB, which performs numerical integration using global adaptive quadrature. This method numerically evaluates the integral of the function  $U_m(\tilde{\tau})$   $U_j(\tilde{\tau})$  over the interval [-1,1]. The global adaptive quadrature algorithm automatically adjusts the number and placement of integration points to ensure accurate and efficient computation of the integral.

The right-hand sides of Eqs. (35)-(38) involve double integrals. The inner integrals of Eqs. (35)-(38) are of the following types:

$$I_{sm} = \int_{-1}^{1} U_m(\tilde{\tau}) \frac{\sqrt{1 - (\tilde{\tau})^2}}{(\tilde{\tau} + \widehat{\mathcal{Z}_{pk}})^s} d\tilde{\tau} \; ; \; s = \{2, 3\} \; \& \; m = \{0, 1, 2, ...n\} \; , \tag{39}$$

in which  $\widehat{\mathcal{Z}_{pk}}$  is located outside the interval [-1,1].

They can be evaluated analytically by employing the following recursive relation between Chebyshev polynomials:

$$U_{m+1}(\widetilde{\tau}) = 2\widetilde{\tau} U_m(\widetilde{\tau}) - U_{m-1}(\widetilde{\tau}).$$
(40)

To use this relation, we have to have closed-form expressions for the integrals with m=0 and m=1. Those expressions are

$$I_{11} = \pi + 2\pi \left(-1 + \sqrt{1 - \frac{1}{(\widehat{\mathcal{Z}_{pk}})^2}}\right) (\widehat{\mathcal{Z}_{pk}})^2,$$
 (41)

$$I_{20} = -\pi - \frac{\widehat{\mathcal{Z}}_{pk} \, \mathcal{I}}{2 \sqrt{1 - (\widehat{\mathcal{Z}}_{pk})^2}}, \qquad (42)$$

$$I_{21} = 4\pi \widehat{\mathcal{Z}_{pk}} + \frac{2 - 4(\widehat{\mathcal{Z}_{pk}})^2}{\sqrt{1 - (\widehat{\mathcal{Z}_{pk}})^2}} \left[ \ln\left(1 - \widehat{\mathcal{Z}_{pk}}\right) - \ln\left(\widehat{\mathcal{Z}_{pk}} - 1\right) \right] , \qquad (43)$$

$$I_{30} = \frac{\mathcal{I}}{4\sqrt{\left(1 - (\widehat{\mathcal{Z}}_{pk})^2\right)^3}},\tag{44}$$

$$I_{31} = 2\left(I_{20} - \widehat{\mathcal{Z}}_{pk} I_{30}\right),$$
 (45)

where,

$$\mathcal{I} = \left[ \ln \left( \frac{1}{\widetilde{\mathcal{Z}_{pk}}} \right) - \ln \left( -\sqrt{\frac{1}{\widetilde{\mathcal{Z}_{pk}}}} \right) + \ln \left( -\sqrt{\widetilde{\mathcal{Z}_{pk}}} \right) \right] , \tag{46}$$

in which  $\widetilde{\mathcal{Z}_{pk}} = \frac{1-\widehat{\mathcal{Z}_{pk}}}{1+\widehat{\mathcal{Z}_{pk}}}$ .

In expressions (42)-(46), proper care has to be taken in evaluations of complex logarithms to ensure that their branch cuts are chosen along the negative real axis.

If the complex variable t is defined as  $t=|t|\exp{(\mathrm{i}\vartheta)}$ , where |t| is its absolute value and  $\vartheta$  is its principal argument  $(-\pi<\vartheta\leq\pi)$ , then the branch cuts of multi-valued logarithmic and square root functions are defined as

$$\sqrt{t} = \sqrt{|t|} \exp(i\vartheta/2), -\pi < \vartheta \le \pi,$$

$$\ln t = \ln |t| + i\vartheta$$
,  $-\pi < \vartheta \le \pi$ .

The value of  $\mathcal{I}$  of Eq. (46) is computed as

$$\mathcal{I} = \begin{cases} 2i\pi & \text{if } \theta \in (-\pi, 0] \\ -2i\pi & \text{if } \theta \in (0, \pi] \end{cases},$$
(47)

in which  $\theta$  is the principal argument of  $\widetilde{\mathcal{Z}}_{pk}$  that belongs to the interval  $(-\pi, \pi]$ .

Similarly, considering that the principal argument  $\phi$  of  $\left(1-\widehat{\mathcal{Z}_{pk}}\right)$  is located within the interval  $(-\pi,\pi]$ , the logarithmic terms in Eq. (43) are computed as

$$\left[\ln\left(1-\widehat{\mathcal{Z}_{pk}}\right)-\ln\left(-(1-\widehat{\mathcal{Z}_{pk}})\right)\right] = \begin{cases} -i\pi & \text{if } \phi \in (-\pi,0]\\ i\pi & \text{if } \phi \in (0,\pi] \end{cases}.$$
(48)

The outer integrals on the right-hand sides of Eqs. (35)-(38) are evaluated numerically by using the 'trapz' function in MATLAB. This function estimates the definite integral of a given set of data points using the trapezoidal rule. The integrals are computed over the interval [-1, 1] at Chebyshev points defined as

$$x_p = \cos\left(\frac{p\pi}{n+1}\right); \quad p = \{1, 2, ..., K\}.$$
 (49)

In the numerical section of this paper, we took K=100.

7.4. Solution of the system and evaluations of elastic fields outside of material surfaces

Once the system of Eqs. (32)-(33) is solved and approximations for  $\widetilde{\sigma}^{S}$  and  $\omega^{S}$  are known, real and imaginary components of  $\Delta \widetilde{\sigma}$  can be found from the relations

$$\operatorname{Re}[(\Delta \widetilde{\sigma})_{j}] = (\widetilde{\sigma}_{0})_{j} \frac{\partial \omega_{j}^{S}}{\partial \widetilde{\tau}},$$

$$\operatorname{Im}[(\Delta \widetilde{\sigma})_{j}] = \frac{\partial \widetilde{\sigma}_{j}^{S}}{\partial \widetilde{\tau}}.$$
(50)

The use of expressions Eq. (50) in Eq. (18) particularized for the case of straight segments, facilitates computation of the displacements within the domain of interest at the points outside L.

The stresses  $\sigma_{kj}(z)$  at those points can be determined by using Eqs. (14)-(15) and Eq. (12), modified for the case of straight segments. To evaluate  $\sigma_{11} + i\sigma_{12}$ , the point z should be chosen on the line such that the normal of the line is parallel to the positive  $x_1$  axis of the Cartesian coordinate system. This choice corresponds to  $d\overline{z}/dz = -1$ . Similarly, to evaluate  $\sigma_{22} - i\sigma_{12}$ , the point z should be chosen on the line such that the normal of a line is parallel

to the positive  $x_2$  axis of the Cartesian coordinate system. This leads to  $d\overline{z}/dz = 1$ .

Strains at the same points can be obtained by using standard Hooke's law as

$$\varepsilon_{11}(z) + \varepsilon_{22}(z) = \frac{\kappa - 1}{4\mu} [\sigma_{11}(z) + \sigma_{22}(z)],$$

$$\varepsilon_{22}(z) - \varepsilon_{11}(z) + 2i\varepsilon_{12}(z) = \frac{1}{2\mu} [\sigma_{22}(z) - \sigma_{11}(z) + 2i\sigma_{12}(z)].$$
(51)

Finally, the stress intensity factors  $K_1$  and  $K_2$  can be evaluated as

$$K_{1} = \lim_{\widetilde{r} \to 0} \widetilde{\sigma}_{22} \sqrt{2\pi \widetilde{r}} ,$$

$$K_{2} = \lim_{\widetilde{r} \to 0} \widetilde{\sigma}_{12} \sqrt{2\pi \widetilde{r}} ,$$

$$(52)$$

where  $\tilde{r}$  is the dimensionalized radial distance from the corresponding tip of the surface and  $\tilde{\sigma}_{ij}$  are asymptotic expansions for the dimensionless stresses in its vicinity.

The asymptotic expansions near the tip  $\tilde{\tau}^0 = 1$  of p-th surface, p = 1, 2, ...N, and the corresponding expressions for the stress intensity factors at that tip were obtained in [35] as

$$\widetilde{\sigma}_{11} = \frac{2}{\sqrt{2\pi\widetilde{r}}(1-\kappa)} \left[ K_2 \sin\frac{\theta}{2} \left( \frac{\kappa-3}{2} - \cos\frac{\theta}{2} \cos\frac{3\theta}{2} \right) + K_1 \cos\frac{\theta}{2} \left( \frac{\kappa+3}{2} - \sin\frac{\theta}{2} \cos\frac{3\theta}{2} \right) \right],$$
(53)

$$\widetilde{\sigma}_{22} = \frac{2}{\sqrt{2\pi\widetilde{r}}(\kappa - 1)} \left[ K_2 \sin\frac{\theta}{2} \left( \frac{\kappa + 1}{2} - \cos\frac{\theta}{2} \cos\frac{3\theta}{2} \right) + K_1 \cos\frac{\theta}{2} \left( \frac{\kappa - 1}{2} - \sin\frac{\theta}{2} \sin\frac{3\theta}{2} \right) \right],$$
(54)

$$\widetilde{\sigma}_{12} = \frac{2}{\sqrt{2\pi\widetilde{r}}(\kappa - 1)} \left[ K_2 \cos\frac{\theta}{2} \left( \frac{\kappa - 1}{2} + \sin\frac{\theta}{2} \sin\frac{3\theta}{2} \right) - K_1 \sin\frac{\theta}{2} \left( \frac{\kappa + 1}{2} + \cos\frac{\theta}{2} \cos\frac{3\theta}{2} \right) \right],$$
(55)

where

$$K_{1} = \frac{\sqrt{\pi}(\kappa - 1)\operatorname{Im}(\sigma_{p}^{*})}{2(1 + \kappa)},$$

$$K_{2} = \frac{\sqrt{\pi}(\kappa - 1)\operatorname{Re}(\sigma_{p}^{*})}{2(1 + \kappa)},$$
(56)

$$\sigma_p^* = -\sum_{m=0}^n \left[ (\widetilde{\sigma_0})_p (B_p)_m + i(A_p)_m \right] (1+m) . \tag{57}$$

Using the limiting procedure similar to that of [35] (see Appendix A for the details), we obtained the expansions for the stresses near the tip  $\tilde{\tau}^0 = -1$  of p-th surface, p = 1, 2, ...N, and the corresponding expressions for the stress intensity factors. They are

$$\widetilde{\sigma}_{11} = \frac{2}{\sqrt{2\pi\widetilde{r}}(1-\kappa)} \left[ K_2 \cos\frac{\theta}{2} \left( \frac{\kappa-3}{2} + \sin\frac{\theta}{2} \sin\frac{3\theta}{2} \right) - K_1 \sin\frac{\theta}{2} \left( \frac{\kappa+3}{2} + \cos\frac{\theta}{2} \cos\frac{3\theta}{2} \right) \right], \tag{58}$$

$$\widetilde{\sigma}_{22} = \frac{2}{\sqrt{2\pi\widetilde{r}}(1-\kappa)} \left[ K_1 \sin\frac{\theta}{2} \left( \frac{\kappa-1}{2} + \cos\frac{\theta}{2} \cos\frac{3\theta}{2} \right) - K_2 \cos\frac{\theta}{2} \left( \frac{\kappa+1}{2} + \sin\frac{\theta}{2} \sin\frac{3\theta}{2} \right) \right], \tag{59}$$

$$\widetilde{\sigma}_{12} = \frac{2}{\sqrt{2\pi\widetilde{r}}(1-\kappa)} \left[ K_2 \sin\frac{\theta}{2} \left( \frac{\kappa-1}{2} - \cos\frac{\theta}{2} \cos\frac{3\theta}{2} \right) + K_1 \cos\frac{\theta}{2} \left( \frac{\kappa+1}{2} - \sin\frac{\theta}{2} \sin\frac{3\theta}{2} \right) \right], \tag{60}$$

where

$$K_{1} = \frac{\sqrt{\pi}(1-\kappa)\operatorname{Im}(\sigma_{p}^{*})}{2(1+\kappa)},$$

$$K_{2} = \frac{\sqrt{\pi}(1-\kappa)\operatorname{Re}(\sigma_{p}^{*})}{2(1+\kappa)},$$
(61)

$$\sigma_p^* = -\sum_{m=0}^n (-1)^{1+m} \left[ (\widetilde{\sigma_0})_p (B_p)_m + i(A_p)_m \right] (1+m) . \tag{62}$$

#### 8. Numerical Results

# 8.1. Validation

We first made sure that, for the cases of Gurtin-Murdoch material surfaces located sufficiently far away from each other, the obtained fields at each surface were consistent with the corresponding results reported in [34] for a matrix material containing a single surface. To do that, we placed two Gurtin-Murdoch surfaces at substantial distances and observed notable agreements with the results depicted in Figs. 5, 6, 8, 9, 11 of [34]. We have also validated the stress intensity factors near the tips of the surfaces by comparison with those reported in Table 1 of the same paper.

Second, we compared our results with the results reported in [15] for the problem involving two rigid line inclusions, each of length 2a arranged either in collinear or parallel configurations. As in the latter paper, we considered the matrix material characterized by E=22 MPa and  $\nu=0.45$ , took the loading conditions to be  $\varepsilon_{11}^{\infty}=0.01$ ,  $\varepsilon_{22}^{\infty}=\varepsilon_{12}^{\infty}=0$ , and assumed that  $\gamma_1=\gamma_2=0$  and  $\widetilde{\sigma}_0=0$ .

In both configurations, the inclusions were separated by the dimensionless distance h/a, as can be seen from Figs. 2, 3, which also present the contours of relative strains in the region surrounding the inclusions. Specifically, Fig. 2 presents the contours of  $\varepsilon_{11}/\varepsilon_{11}^{\infty}$  for the collinear configurations with h/a=2, Fig. 2a, and h/a=0.2, Fig. 2b. Similarly, Fig. 3 presents the contours of  $\varepsilon_{11}/\varepsilon_{11}^{\infty}$  for the parallel configuration with h/a=1, Fig. 3a, and h/a=0.5, Fig. 3b.

Comparing those two figures with Figs. 12, 13 of [15], we can conclude that there is a satisfactory qualitative agreement between our results and those presented in [15].

In [15], the authors also presented the results for the relative strain intensity factor  $K_{\epsilon}/K_{\epsilon}^{\text{Single}}$  that, for rigid line inclusions, can be expressed via the corresponding relative stress intensity factor as

$$\frac{K_1}{K_1^{\text{Single}}} = \frac{K_{\epsilon}}{K_{\epsilon}^{\text{Single}}} \,, \tag{63}$$

in which  $K_1$  is the Mode I stress intensity factor for a system with two rigid line inclusions,  $K_1^{\text{Single}}$  is that for a single rigid line, and  $K_{\epsilon}$ ,  $K_{\epsilon}^{\text{Single}}$  are the

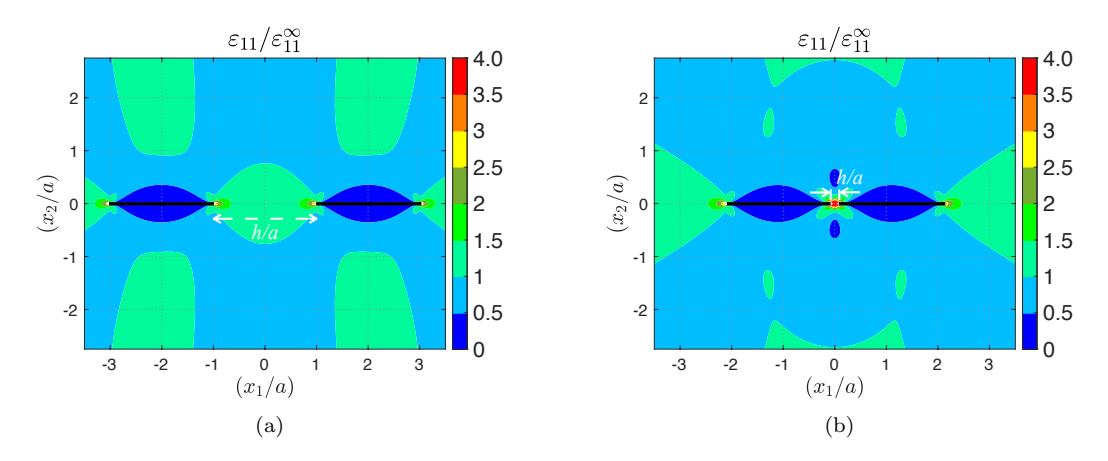


**Fig. 2.** Normalized strain  $\varepsilon_{11}/\varepsilon_{11}^{\infty}$  for the collinear configuration: (a) h/a=2 (left) and (b) h/a=0.2 (right).

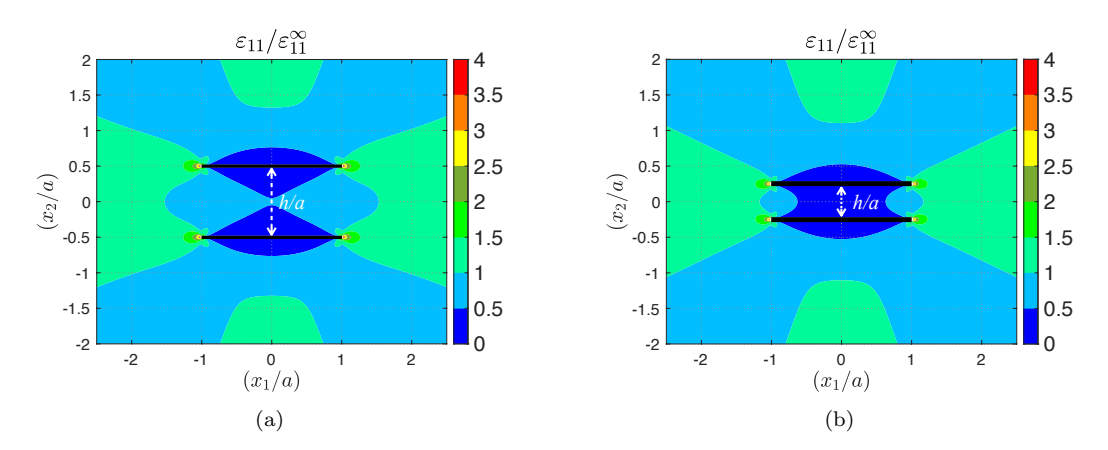


**Fig. 3**. Normalized strain  $\varepsilon_{11}/\varepsilon_{11}^{\infty}$  for the parallel configuration: (a) h/a=1 (left) and (b) h/a=0.5 (right).

corresponding strain intensity factors. Using relation (63), we compared our results to those presented in Figs. 17, 18 of [15] and obtained satisfactory qualitative agreement.

#### 8.2. Selected Parametric Studies

As the parametric space for our problem is quite large, in this section, we focus on the studies of the effects due to the locations and orientations of the surfaces, as well as on the influences of the dimensionless parameters  $\gamma$  and  $\tilde{\sigma}_0$ . For these studies, we selected three distinct configurations of N surfaces of equal sizes of 2a, as illustrated in Fig. 4.

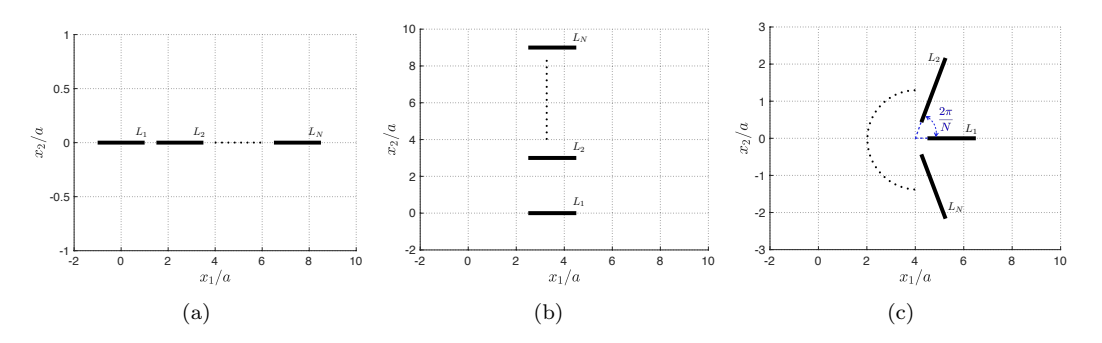


Fig. 4. (a) Collinear configuration, (b) Parallel configuration, (c) Radial configuration.

We considered the material composed of an epoxy matrix reinforced by the graphene-oxide nanoplatelets. The elastic properties of the material were taken from [44]. The epoxy matrix was considered to be isotropic and characterized by  $\mu=2$  GPa,  $\nu=0.35$ . The dimensionless parameters for each surface were set as  $\gamma=0.12$ ,  $\widetilde{\sigma}_0=0.025$ , and the only non-zero applied loading was taken to be  $\widetilde{\sigma}_{22}^{\infty}=0.05$ . To study the influence of the dimensionless parameters,  $\gamma$  and  $\widetilde{\sigma}_0$  more rigorously, we considered wider intervals of variations of those parameters. Based on the results of convergence studies, we obtained the numerical results using our approach with 20 terms in the Chebyshev series and 100 points in the Gaussian quadrature.

Collinear configuration with three surfaces Here, we examine the effects of surface tension and the influence of interactions based on the locations of the three surfaces,  $L_1$ ,  $L_2$ , and  $L_3$ , in the collinear configuration. The surfaces are separated from one another by the normalized distance denoted by  $\tilde{h} = h/a$ , see Fig. 5.

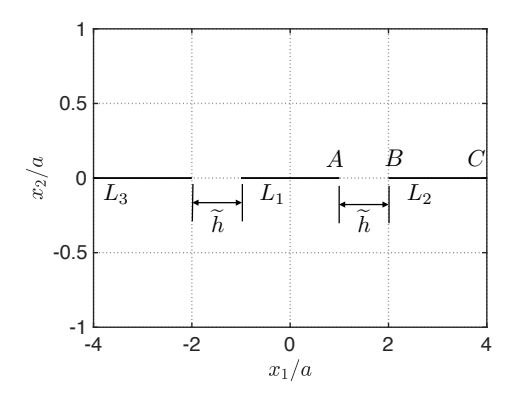
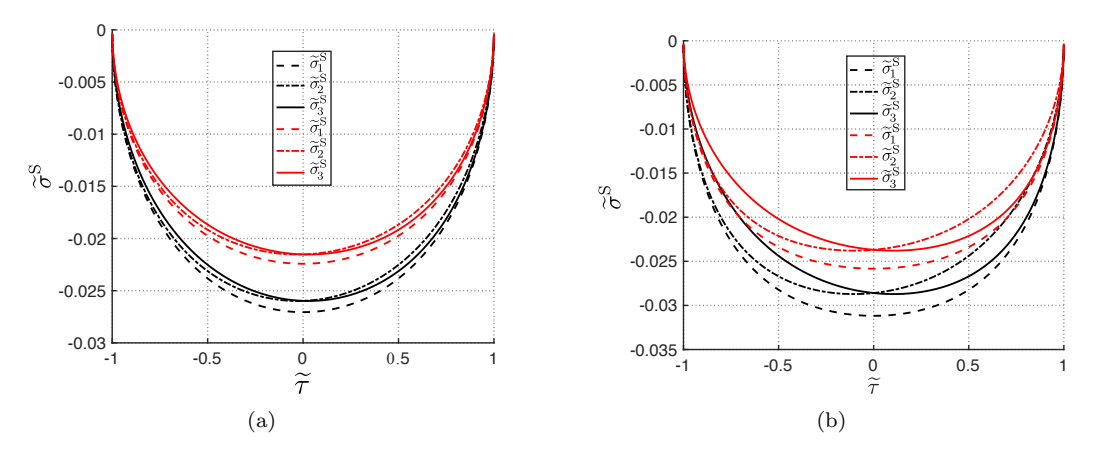


Fig. 5. Collinear configuration.

Fig. 6 presents the plots of the distribution of  $\widetilde{\sigma}^S$  along each surface for specified values of  $\widetilde{h}$  selected to be  $\widetilde{h}=1,0.25$ . For comparison purposes, we also consider the case of  $\widetilde{\sigma}_0=0, \ \gamma=0.012$  for each surface.



**Fig. 6.** Distribution of  $\widetilde{\sigma}^S$  along each surface for  $\widetilde{\sigma}_0 = 0$  (Black) and  $\widetilde{\sigma}_0 = 0.025$  (Red): (a)  $\widetilde{h} = 1$ , (b)  $\widetilde{h} = 0.25$ .

As the surfaces are equally spaced from each other, it was anticipated that the distribution of  $\tilde{\sigma}^{S}$  along the  $L_1$  surface would exhibit symmetry around  $\tilde{\tau} = 0$ , while the distribution of  $\tilde{\sigma}^{S}$  along the  $L_2$ , and  $L_3$  might lack symmetry around  $\tilde{\tau} = 0$ . The interval  $\tilde{\tau} = [0, 1]$  of the  $L_3$  surface was expected to be influenced by the  $L_1$  surface, and similarly, the interval  $\tilde{\tau} = [-1, 0]$  of the  $L_2$  surface was anticipated to be influenced by the  $L_1$  surface. Additionally, it was also anticipated that, as the surfaces move farther apart from each other, the distributions of  $\tilde{\sigma}^{S}$  along each surface would converge towards the

distribution of  $\tilde{\sigma}^{S}$  corresponding to the matrix material containing a single surface. All these expectations have been met, as demonstrated by the plots of Fig. 6.

From Fig. 6, it can also be seen that the presence of surface tension leads to decrease in the magnitudes of  $\tilde{\sigma}^S$ . To understand this phenomenon, we considered two scenarios of loading conditions. In the first scenario, we assumed zero surface tension and accounted for the influence of external loading, while in the second scenario, we only considered the effect of surface tension and assumed zero external loading. In the first scenario,  $\tilde{\sigma}^S$  was compressive, while, in the second scenario,  $\tilde{\sigma}^S$  was tensile. That explains the reduction in the magnitudes of  $\tilde{\sigma}^S$  mentioned above.

Under chosen geometrical arrangement, material parameters, and loading conditions, the only nonzero complex constant of Eq. (29) is  $C_{3p}^{(\omega_k)}$ . Taking that into account, it is clear that  $\omega^{\rm S}=0$  is the only trivial solution of Eq. (29). Therefore, the plots of  $\omega^{\rm S}$  do not need to be presented for this case.

Table 1 Stress intensity factor  $K_1$  at various tips for collinear configuration as function of  $\widetilde{h}$ .

	No Surface Tension		With Surface Tension			
$\widetilde{h}$	$(K_1)_A$	$(K_1)_B$	$(K_1)_C$	$(K_1)_A$	$(K_1)_B$	$(K_1)_C$
$\widetilde{h} = 10.0$	0.0052	0.0052	0.0052	0.0043	0.0043	0.0043
$\widetilde{h} = 3.0$	0.0054	0.0053	0.0053	0.0045	0.0044	0.0044
$\widetilde{h} = 1.0$	0.0059	0.0058	0.0055	0.0049	0.0047	0.0045
$\widetilde{h} = 0.5$	0.0066	0.0065	0.0057	0.0055	0.0054	0.0047
$\widetilde{h} = 0.25$	0.0087	0.0077	0.0075	0.0064	0.0062	0.0048

In Table 1, we present the results for the Mode I stress intensity factor  $K_1$  at the tips A, B, and C shown in Fig. 5. It can be concluded that the value of  $K_1$  increases with the decrease of the normalized distance  $\widetilde{h}$ . It can also be seen that the values of  $K_1$  for the case of non-zero surface tension are smaller than those for the case of vanishing surface tension. Naturally, the values of  $K_1$  are larger at the tips that are located closer to each other. The increase in the value of  $K_1$  is more pronounced at tip A, followed by tip B, and then by tip C. Under the given geometry, material properties, and applied loading

conditions, the values of the Mode II stress intensity factor  $K_2$  at all tips are found to be zero both in the presence and absence of surface tension. Additionally, it was observed that the interactions between the surfaces in the collinear configuration do not play a role when the distances between them become roughly five times larger than the half of their lengths.

Parallel configuration with three surfaces Now, we perform similar analysis for the parallel configuration involving three surfaces,  $L_1$ ,  $L_2$ , and  $L_3$ . We maintain the same loading conditions and material properties as in the case of collinear configuration. The same symbol  $\tilde{h}$  is used to characterize the normalized vertical separation distance between the neighboring surfaces, as shown in Fig. 7.

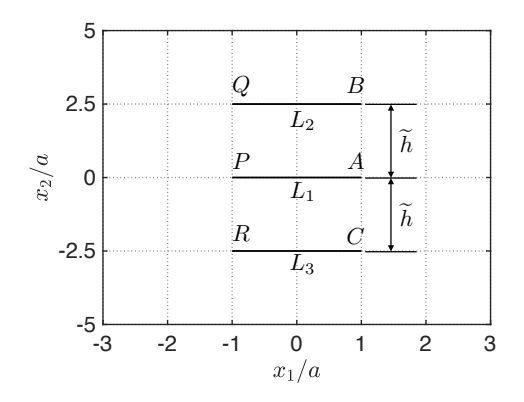
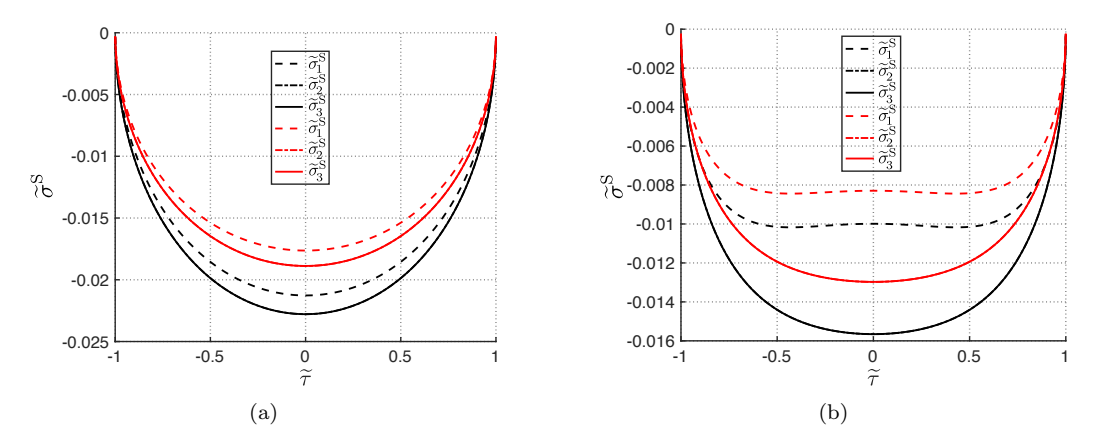


Fig. 7. Parallel configuration.

Figs. 8-9 present the plots of the distribution of  $\widetilde{\sigma}^S$  and  $\omega^S$  along each surface for two values of  $\widetilde{h}$  selected to be  $\widetilde{h}=1,0.25$ . For comparison purposes, we also consider the case of  $\widetilde{\sigma}_0=0$  for each surface and, as before, take  $\gamma=0.012$ .

As the three surfaces are arranged in a manner that assures geometric symmetry, it was expected that the distribution of  $\tilde{\sigma}^{S}$  and  $\omega^{S}$  along all three surfaces would display symmetry around  $\tilde{\tau}=0$ . Additional anticipation was that, with increasing value of  $\tilde{h}$ , the distributions of  $\tilde{\sigma}^{S}$  and  $\omega^{S}$  along each surface would gradually approach the distributions corresponding to a matrix material containing a single surface. These expectations have been met, as illustrated by the plots of Figs. 8, 9. It can be seen from Figs. 8-9 that the presence of surface tension leads to a decrease in the magnitudes of  $\tilde{\sigma}^{S}$  and



**Fig. 8.** Distribution of  $\widetilde{\sigma}^S$  along each segment for  $\widetilde{\sigma}_0 = 0$  (Black) and  $\widetilde{\sigma}_0 = 0.025$  (Red): (a)  $\widetilde{h} = 1$ , (b)  $\widetilde{h} = 0.25$ .

 $\omega^{S}$ . This phenomenon has been explained in detail in the case of collinear configuration.

Figs. 8b and 9b also provide insights into how the interaction between the surfaces affects the behavior of  $\tilde{\sigma}^S$  and  $\omega^S$  in the vicinity of the mid-zones of the surfaces.

Table 2 Stress intensity factor  $K_1$  at various tips for parallel configuration as function of  $\widetilde{h}$ .

	No Surface Tension		With Surface Tension	
$\widetilde{h}$	$(K_1)_A$	$(K_1)_B = (K_1)_C$	$(K_1)_A$	$(K_1)_B = (K_1)_C$
$\widetilde{h} = 10.0$	0.0052	0.0052	0.0043	0.0043
$\widetilde{h} = 3.0$	0.0052	0.0052	0.0043	0.0043
$\widetilde{h} = 1.0$	0.0045	0.0048	0.0037	0.0040
$\widetilde{h} = 0.5$	0.0038	0.0043	0.0032	0.0036
$\widetilde{h} = 0.25$	0.0034	0.0040	0.0028	0.0033

In Table 2, we present the values of  $K_1$  at the tips A, B, and C, see Fig. 7, for various values of  $\widetilde{h}$ . Given the geometric and material symmetry of the system under the specified loading conditions, we can infer that the values of  $K_1$  at the tips B and C are equal, and the values of  $K_1$  at the tips P,

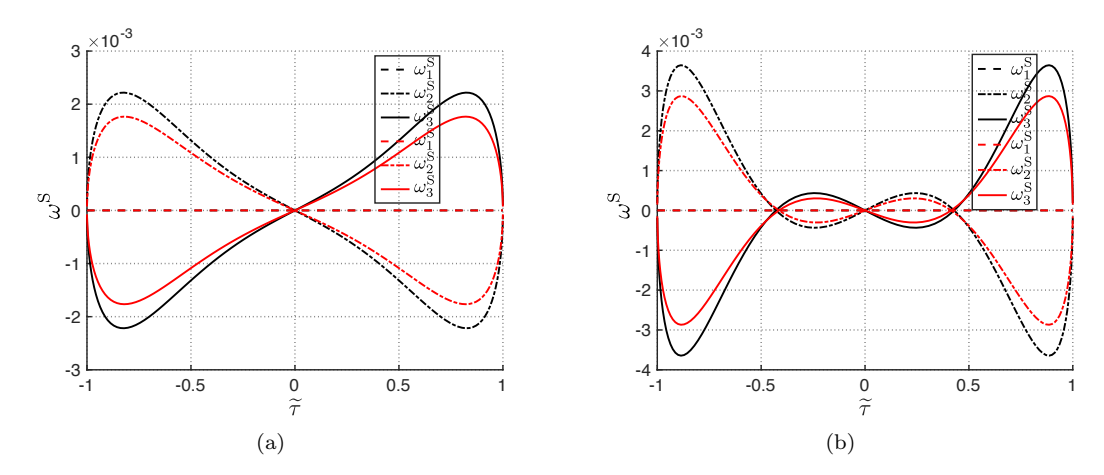


**Fig. 9.** Distribution of  $\omega^{S}$  along each segment for  $\widetilde{\sigma}_{0} = 0$  (Black) and  $\widetilde{\sigma}_{0} = 0.025$  (Red): (a)  $\widetilde{h} = 1$ , (b)  $\widetilde{h} = 0.25$ .

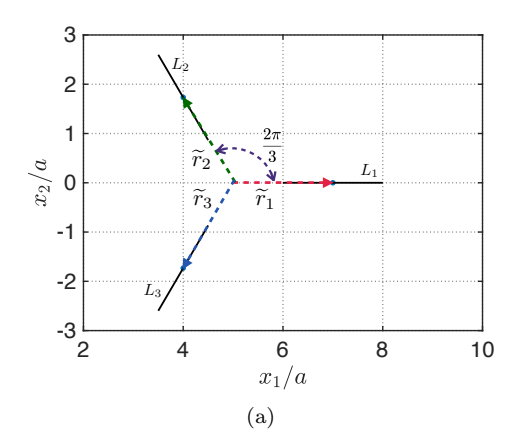
Q, and R are identical to those at the tips A, B, and C, respectively. We can conclude from the data of Table 2 that, when the surfaces approach each other, the value of  $K_1$  associated with each surface decreases in both cases (with and without surface tension), which manifests shielding effects of this particular geometrical arrangement. Also, in the case of non-zero surface tension, the values of  $K_1$  related to each surface are smaller than that for the case of vanishing surface tension, indicating that, as in the case of collinear configuration, the residual surface tension reduces stress concentrations at the tips.

In Table 3, we present the values of  $K_2$  at the tips B, C, Q, and R, see Fig. 7, for the case of non-vanishing surface tension. The values of  $K_2$  at tips A and P are practically zero; thus, they are not presented in the table. From the analyses of the data of Table 3, it becomes evident that the absolute value of  $K_2$  increases as the surfaces come closer to each other. This trend is opposite to that for the values of  $K_1$  observed in Table 2. However, the absolute values of  $K_1$  are a few orders of magnitude larger than those of  $K_2$ . Under the given geometry, material properties, and applied loading conditions,  $K_2 = 0$  at all tips for the case when  $\tilde{\sigma}_0 = 0$ . It was also observed that, in the parallel configuration, the effects of interactions disappear when the distances between the surfaces become roughly four times larger than the half of their lengths.

Table 3 Stress intensity factor  $K_2$  at various tips for parallel configuration as function of  $\widetilde{h}$  for non-zero surface tension.

$\widetilde{h}$	$(K_2)_B = -(K_2)_C$	$(K_2)_Q = -(K_2)_R$
$\widetilde{h} = 10.0$	4.9305e-07	-1.7823e-07
$\widetilde{h} = 3.0$	1.1956e-05	-4.3895e-06
$\widetilde{h} = 1.0$	6.0941 e-05	-2.3464e-05
$\widetilde{h} = 0.5$	8.6487e-05	-3.6469e-05
$\widetilde{h} = 0.25$	1.0950e-04	-4.6754e-05

Radial configuration with three surfaces To establish a radial arrangement, we select a random point within some domain to act as the center of a circle. The notation  $\tilde{r}_j$  signifies the normalized radial distance between that point and the mid-point of the j-th surface. It is assumed that  $\tilde{r}_1 = \tilde{r}_2 = \tilde{r}_3 = \tilde{r}$ . Additionally, the angle between the adjacent surfaces is  $2\pi/N$ , where N represents the number of surfaces, N=3 in our specific case, as shown in Fig. 10a.



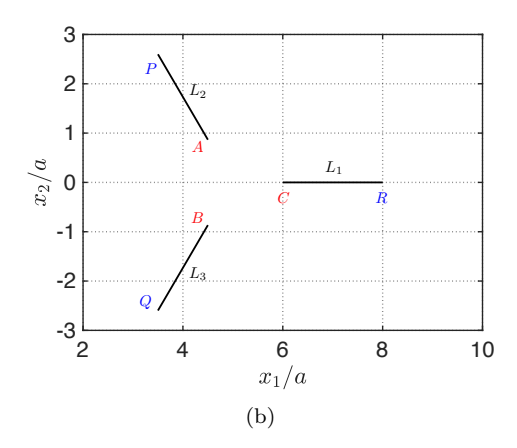
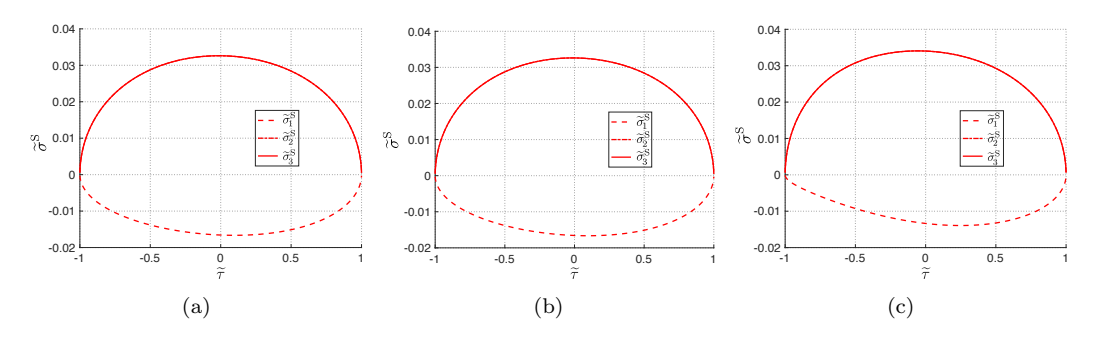


Fig. 10. Radial configuration with three surfaces a) geometrical arrangement, b) adopted notations for the tips of the surfaces.

Study of influence of interactions: We assume the same loading conditions,  $\tilde{\sigma}_{22}^{\infty} = 0.05$ , and the same surface parameters:  $\gamma = 0.12$ ,  $\tilde{\sigma}_0 = 0.025$ , as in Subsection 8.2 and vary the values of  $\tilde{r}$  to study the effects of inter-

actions. As the distance between the surfaces increases, the level of interactions diminishes, and conversely, as they approach each other, interactions become more pronounced. To visualize these effects, we provide the plots of distributions of  $\tilde{\sigma}^{S}$  and  $\omega^{S}$  along each surface generated for specific values of  $\tilde{r} = 1.5, 1.25, 1.125$ , see Figs. 11- 12.



**Fig. 11**. Distribution of  $\widetilde{\sigma}^S$  along each segment for: (a)  $\widetilde{r}=1.5$ , (b)  $\widetilde{r}=1.25$ , (c)  $\widetilde{r}=1.125$ .

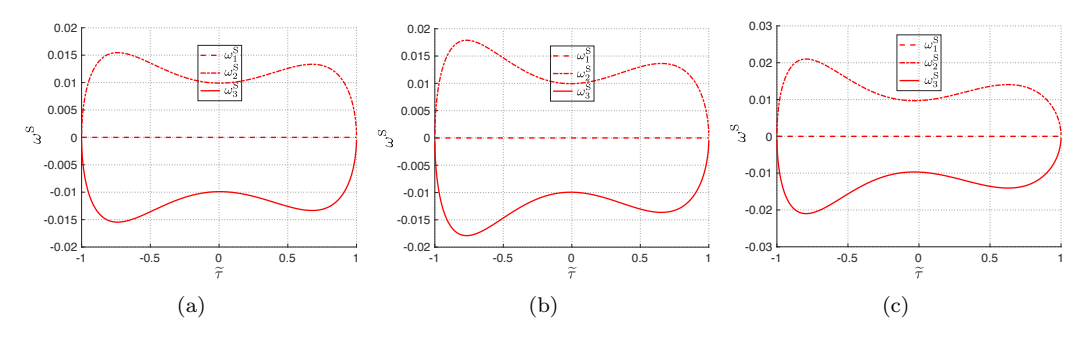


**Fig. 12**. Distribution of  $\omega^S$  along each segment for: (a)  $\tilde{r}=1.5$ , (b)  $\tilde{r}=1.25$ , (c)  $\tilde{r}=1.125$ .

Notably, in Fig. 11, significant change in the curvature of the  $\widetilde{\sigma}_1^{\rm S}$  plots and the emergence of symmetry-breaking patterns in the plots for  $\widetilde{\sigma}^{\rm S}$  can be observed, as one transitions from Fig. 11a to Fig. 11c. This trend becomes apparent as the surfaces draw closer to each other. Likewise, as the surfaces approach each other, the effects of interactions become increasingly evident, leading to symmetry-breaking patterns around  $\widetilde{\tau}=0$  for  $\omega_2^{\rm S}$  and  $\omega_3^{\rm S}$ , as one transitions from Fig. 12a to Fig. 12c.

To further showcase the effects of interactions, in Table 4, we present the values of  $K_1$  at the tips A, B, C, P, Q, and R, see Fig. 10b. Due to

Table 4 Stress intensity factor  $K_1$  at various tips for radial configuration as function of  $\widetilde{r}$ .

$\widetilde{r}$	$(K_1)_A = (K_1)_B$	$(K_1)_C$	$(K_1)_P = (K_1)_Q$	$(K_1)_R$
$\widetilde{r} = 2.5$	-0.0068	0.0040	-0.0069	0.0041
$\widetilde{r} = 2.0$	-0.0069	0.0037	-0.0069	0.0040
$\widetilde{r} = 1.5$	-0.0071	0.0032	-0.0070	0.0038
$\widetilde{r} = 1.3$	-0.0073	0.0026	-0.0070	0.0037
$\widetilde{r} = 1.15$	-0.0077	0.0016	-0.0071	0.0035

Table 5
Stress intensity factor  $K_2$  at various tips for radial configuration as function of  $\widetilde{r}$ .

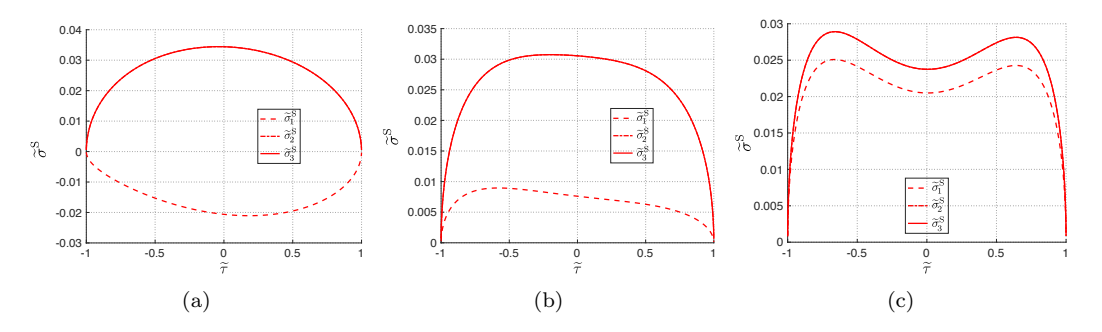
$\overline{\widetilde{r}}$	$(K_2)_A = -(K_2)_B$	$(K_2)_P = -(K_2)_Q$
$\widetilde{r} = 2.5$	-1.4200e-04	-4.4610e-04
$\widetilde{r} = 2.0$	-1.4962e $-04$	-4.4879e-04
$\widetilde{r} = 1.5$	-1.7311e-04	-4.5300e-04
$\widetilde{r} = 1.3$	-2.0007e-04	-4.5549e-04
$\widetilde{r} = 1.15$	-2.4769e-04	-4.5829e-04

the geometric and material symmetry within the system, under the specified loading conditions, we can deduce that the absolute values of  $K_1$  at the tips A and B are identical. The same is true for the absolute values of  $K_1$  at the tips P and Q. Analysis of Table (4) reveals that, as the surfaces draw closer to each other, the absolute values of  $K_1$  at the tips A, P of  $L_2$  and B, Q of  $L_3$  are increasing, whereas those at the tips C, R of  $L_1$  decrease. Furthermore, the reduction in the values of  $K_1$  at the tip C is more substantial than that at the tip R. Conversely, the increase in the values of  $K_1$  at the tips A and B is larger than that at the tips P and Q.

In Table 5, we present the results for the stress intensity factor  $K_2$  at the tips A, B, P, and Q shown in Fig. 10b. As the values of  $K_2$  at the tips C and R are practically zero, they are not presented in the table. It is observed from Table 5 that, as the surfaces approach each other, the absolute values of  $K_2$  increase. Under the given geometry, material properties, and applied loading conditions,  $K_2 = 0$  at all tips when  $\tilde{\sigma}_0 = 0$ . Additionally, it was observed that the surfaces in the radial configuration are interacting with each other when the distances between them become smaller than roughly four times the half of their lengths.

Given that the effects of interaction are more pronounced when  $\tilde{r} = 1.125$ , we choose to maintain this value of  $\tilde{r}$  for further investigations into the influences of dimensionless surface parameters  $\gamma$  and  $\tilde{\sigma}_0$ .

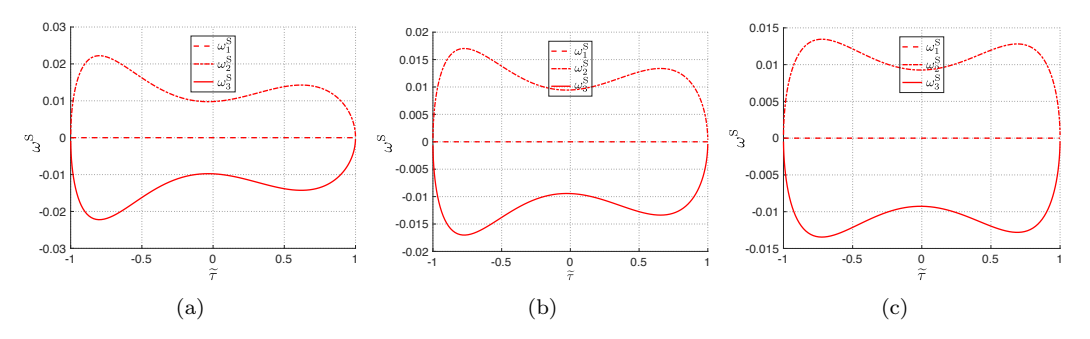
Study of influence of  $\gamma$ : To perform this study, we retain the loading conditions used previously and assume that  $\tilde{\sigma}_0 = 0.025$  and  $\tilde{r} = 1.125$ . Additionally, we vary the parameter  $\gamma$  to attain the following values:  $\gamma = 0, 1, 10$ . In Figs. 13 and 14, we present the plots of  $\tilde{\sigma}^S$  and  $\omega^S$  corresponding to these values of  $\gamma$ .



**Fig. 13.** Distribution of  $\tilde{\sigma}^{S}$  along each segment for: (a)  $\gamma = 0$ , (b)  $\gamma = 1$ , (c)  $\gamma = 10$ .

As the value of  $\gamma$  increases, we can observe the development of symmetry-

building patterns in the distributions of  $\widetilde{\sigma}^S$  and  $\omega^S$  along all surfaces, particularly about  $\widetilde{\tau}=0$ , as shown in Fig. 13-Fig. 14. Additionally, with an increasing value of  $\gamma$ , it is clearly seen from Fig. 13 that the behavior of  $\widetilde{\sigma}_1^S$  changes from compressive to tensile.



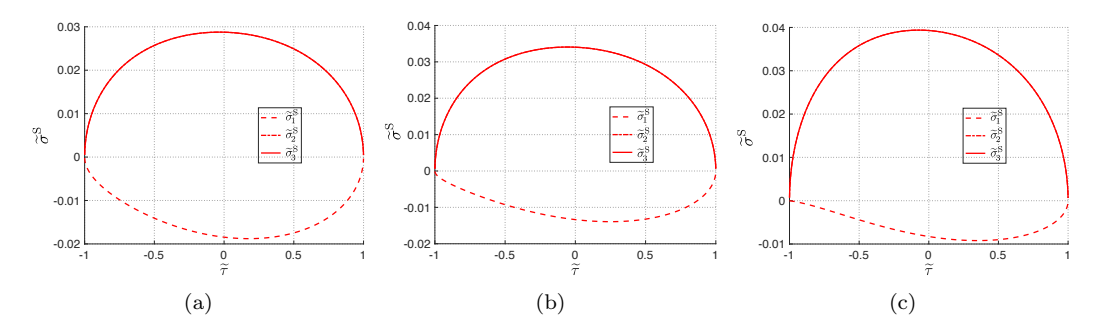
**Fig. 14.** Distribution of  $\omega^{S}$  along each segment for: (a)  $\gamma = 0$ , (b)  $\gamma = 1$ , (c)  $\gamma = 10$ .

Table 6 Stress intensity factor  $K_1$  at various tips for radial configuration as function of  $\tilde{r}$  at  $\gamma = 0$ .

$\widetilde{r}$	$(K_1)_A = (K_1)_B$	$(K_1)_C$	$(K_1)_P = (K_1)_Q$	$(K_1)_R$
$\widetilde{r} = 2.5$	-0.0067	0.0055	-0.0067	0.0056
$\widetilde{r} = 2.0$	-0.0067	0.0052	-0.0067	0.0055
$\widetilde{r} = 1.5$	-0.0068	0.0046	-0.0067	0.0052
$\widetilde{r} = 1.3$	-0.0070	0.0040	-0.0068	0.0051
$\widetilde{r} = 1.15$	-0.0074	0.0030	-0.0069	0.0049

Table 6 presents the values of  $K_1$  at the tips A, B, C, P, Q, and R shown in Fig. 10b for various values of  $\tilde{r}$  under the condition of  $\gamma = 0$ . Comparing Table 4, which corresponds to  $\gamma = 0.12$ , with Table 6 for  $\gamma = 0$ , it is observed that the absolute values of  $K_1$  at tips C and R decrease at a slower rate for the lower value of  $\gamma$ . Additionally, the absolute values of  $K_1$  at the tips A, B, P, and Q increase at a slower rate for the smaller value of  $\gamma$ .

Study of influence of  $\widetilde{\sigma}_0$ : To perform this study, we maintained the same loading conditions and took  $\widetilde{r} = 1.125$ ,  $\gamma = 0.12$ . To examine the influence of  $\widetilde{\sigma}_0$ , we took the values of  $\widetilde{\sigma}_0$  to be  $\widetilde{\sigma}_0 = 0, 0.025, 0.05$ . Fig. 15 presents the distributions of  $\widetilde{\sigma}^S$ .



**Fig. 15.** Distribution of  $\tilde{\sigma}^S$  along each segment for: (a)  $\tilde{\sigma}_0 = 0$ , (b)  $\tilde{\sigma}_0 = 0.025$ , (c)  $\tilde{\sigma}_0 = 0.05$ .

From Fig. 15, it becomes evident that, as the values of  $\tilde{\sigma}_0$  increase, more significant changes are observed in the distribution of  $\tilde{\sigma}^S$  inside the interval  $\tilde{\tau} = [-1, 0]$  of the surface  $L_1$  than inside the corresponding interval  $\tilde{\tau} = [0, 1]$ . Additionally, as the value of  $\tilde{\sigma}_0$  increases, the tensile nature of  $\tilde{\sigma}^S$  becomes more prominent. This shift is characterized by an increase in the magnitude of tensile surface stress  $\tilde{\sigma}^S$  along the surfaces  $L_2$  and  $L_3$  accompanied by a reduction in the magnitude of compressive  $\tilde{\sigma}^S$  for the surface  $L_1$ . However, no significant changes were observed in the plots of  $\omega^S$ .

Table 7 Stress intensity factor  $K_1$  at various tips for radial configuration as function of  $\widetilde{r}$  at  $\widetilde{\sigma}_0 = 0$ .

$\overline{\widetilde{r}}$	$(K_1)_A = (K_1)_B$	$(K_1)_C$	$(K_1)_P = (K_1)_Q$	$(K_1)_R$
$\widetilde{r} = 2.5$	-0.0059	0.0049	-0.0060	0.0050
$\widetilde{r} = 2.0$	-0.0059	0.0047	-0.0060	0.0049
$\widetilde{r} = 1.5$	-0.0060	0.0042	-0.0060	0.0048
$\widetilde{r} = 1.3$	-0.0061	0.0037	-0.0060	0.0046
$\widetilde{r} = 1.15$	-0.0064	0.0029	-0.0061	0.0045

In Table 7, we present the results for the stress intensity factor  $K_1$  at the tips A, B, C, P, Q, and R shown on Fig. 10b, assuming that  $\tilde{\sigma}_0 = 0$ . From the analysis of Table 7, we can observe that, when  $\tilde{r}$  decreases, the absolute values of  $K_1$  at the tips of inclined surfaces,  $L_2$  and  $L_3$ , increase, while the corresponding values at the tips of the horizontal surface,  $L_1$ , decrease. Ad-

ditionally, while comparing the results recorded in Tables 7 and 4, we could see that, the absolute values of  $K_1$  change at slower rate when  $\tilde{\sigma}_0 = 0$ . Under the given geometry, material properties, and applied loading conditions,  $K_2 = 0$  at all tips when  $\tilde{\sigma}_0 = 0$ .

# 8.3. Comparison of the relative Von-Mises stresses for different geometrical arrangements and shear far-field load

In previous sections, we exclusively studied the case of uniaxial far-field loading conditions. Now, we study the influence of loading conditions by comparing the behavior of relative Von-Mises stresses under the uniaxial loading  $\widetilde{\sigma}_{22}^{\infty}=0.05$  and under the shear loading  $\widetilde{\sigma}_{12}^{\infty}=0.05$  for the three arrangements of Fig. 4. For this study, we set the remaining surface parameters as  $\gamma=0.12$  and  $\widetilde{\sigma}_0=0.025$ . Fig. 16 through Fig. 18 display the plots of the relative Von-Mises stresses,  $\widetilde{\sigma}_v/\widetilde{\sigma}_v^{\infty}$ , in the vicinity of the surfaces for the two cases of far-field load and for each of the three arrangements.

The Von-Mises stress, normalized with respect to the shear modulus  $\mu$ , is defined as follows:

$$\widetilde{\sigma}_{v} = \sqrt{\frac{1}{2} \left[ (\widetilde{\sigma}_{11} - \widetilde{\sigma}_{22})^{2} + (\widetilde{\sigma}_{22} - \widetilde{\sigma}_{33})^{2} + (\widetilde{\sigma}_{33} - \widetilde{\sigma}_{11})^{2} \right] + 3(\widetilde{\sigma}_{12})^{2}},$$

$$\widetilde{\sigma}_{33} = \nu(\widetilde{\sigma}_{11} + \widetilde{\sigma}_{22}),$$
(64)

and  $\tilde{\sigma}_v^{\infty}$  is defined by Eq. (64) in which the stress components are taken to be equal to those due to the loading of the homogeneous matrix without the surfaces.

In Figs. 16 and 17, the contour plots of  $\tilde{\sigma}_v/\tilde{\sigma}_v^{\infty}$  are shown for the surfaces in the collinear and parallel configurations, respectively, with  $\tilde{h}=0.25$ . In both cases, the system's response is symmetric for uniaxial loading and antisymmetric for shear loading. For both configurations, intervals of variation of  $\tilde{\sigma}_v/\tilde{\sigma}_v^{\infty}$  for uniaxial load is much wider than that for the shear load. The values of  $\tilde{\sigma}_v/\tilde{\sigma}_v^{\infty}$  are significantly larger for the former type of loading than for the latter one and, in both cases, maximum values occur near the tips.

In Fig. 18, the contour plots of  $\widetilde{\sigma}_v/\widetilde{\sigma}_v^\infty$  are shown for the surfaces arranged in the radial configuration with  $\widetilde{r}=1.125$ . Notably, the intervals of variation of  $\widetilde{\sigma}_v/\widetilde{\sigma}_v^\infty$  for both cases (uniaxial loading and shear loading) are much wider and the values of  $\widetilde{\sigma}_v/\widetilde{\sigma}_v^\infty$  are dramatically larger than the corresponding intervals and values observed for the collinear and parallel configurations. The maximum values of  $\widetilde{\sigma}_v/\widetilde{\sigma}_v^\infty$  occur near the tips of the inclined surfaces.

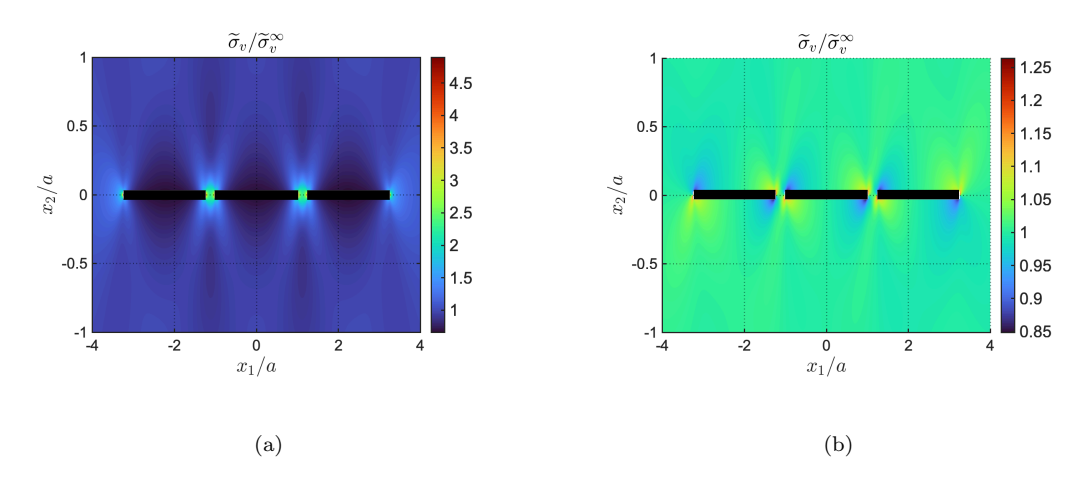


**Fig. 16**. Distribution of  $\tilde{\sigma}_v/\tilde{\sigma}_v^\infty$  in the vicinity of surfaces in collinear configuration with  $\tilde{h}=0.25$ , for: a) uniaxial tension,  $\tilde{\sigma}_{22}=0.05$  b) pure shear,  $\tilde{\sigma}_{12}=0.05$ .

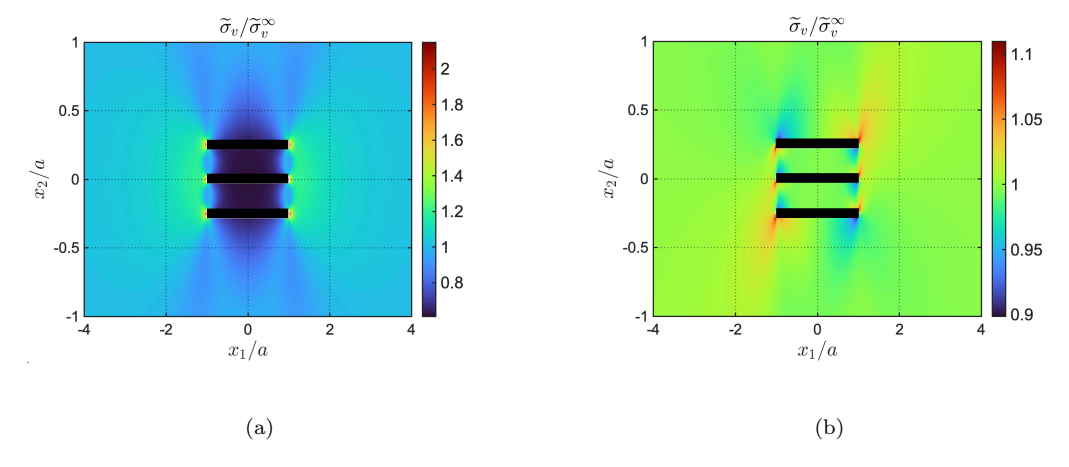


**Fig. 17**. Distribution of  $\tilde{\sigma}_v/\tilde{\sigma}_v^\infty$  in the vicinity of surfaces in parallel configuration with  $\tilde{h}=0.25$ , for: a) uniaxial tension,  $\tilde{\sigma}_{22}=0.05$  b) pure shear,  $\tilde{\sigma}_{12}=0.05$ .

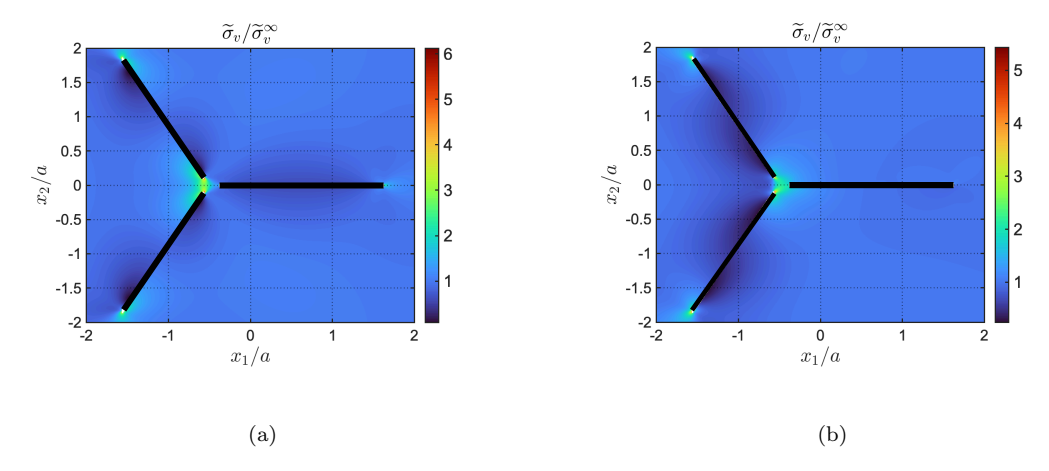


**Fig. 18.** Distribution of  $\widetilde{\sigma}_v/\widetilde{\sigma}_v^{\infty}$  in the vicinity of surfaces in radial configuration with  $\widetilde{r}=1.125$ , for: a) uniaxial tension,  $\widetilde{\sigma}_{22}=0.05$  b) pure shear,  $\widetilde{\sigma}_{12}=0.05$ .

When comparing Figs. 16, 17, and 18, it is evident that the interval variation of  $\tilde{\sigma}_v/\tilde{\sigma}_v^{\infty}$  in narrower and the maximum values of  $\tilde{\sigma}_v/\tilde{\sigma}_v^{\infty}$  are smaller for the parallel configuration, as compared to those for the collinear and radial configurations under both uniaxial and shear loading conditions.

#### 9. Conclusion

In this paper, we studied the plane strain problem of an infinite isotropic elastic matrix containing multiple thin, stiff, and prestressed inhomogeneities /layers along the straight segments. We adopted the Gurtin-Murdoch model of material surface, which treats these inhomogeneities/layers as the vanishing thickness membranes characterized by surface tension and surface elasticity. As the theory is based on the assumption of continuity of displacements and jumps in tractions across the membranes, we adopted the classical tool of a single-layer elastic potential that allows for the fulfillment of the above conditions and for the exact integral representations for the local fields in the entire material domain in terms of the two unknown components of the surface stress tensor. Those components were approximated by the series of Chebyshev polynomials of second-kind multiplied by the weight functions to satisfy the tip conditions automatically. We presented closed-form expressions for the stress intensity factors at the tips of the membranes. The comparison with the available benchmark solutions provided confidence in the proposed theory and numerical algorithm. We conducted a comprehensive study of the influences of various problem parameters for the three geometrical configurations of three membranes.

In the collinear configuration, under uniaxial loading, several trends were observed. Firstly, the absolute values of the Mode I stress intensity factor increased with a decrease in the normalized separation distance. Secondly, the absolute values of that factor were larger in the case of vanishing surface tension. Lastly, the Mode II stress intensity factor was zero in both cases, with and without surface tension.

In the parallel configuration under uniaxial loading, a shielding effect was apparent, which manifested in decrease in the absolute values of the Mode I stress intensity factor with a decrease in normalized separation distance. Similarly, as for collinear configuration under the same loading, larger absolute values of that factor were observed in the case of vanishing surface tension as compared to that with non-zero surface tension. Moreover, for the case of non-vanishing surface tension, non-zero values of Mode II stress intensity factor were obtained at some tips.

The level of stress concentration for the radial configuration, under uniaxial loading, was significantly higher than for the rest of studied configurations, with larger absolute values of the Mode I stress intensity factors at the tips of the horizontal surface than those at the tips of the inclined surfaces. Furthermore, the former values decreased with decreasing normalized radial distance, while the latter values increased. As anticipated, the absolute values of those factors were larger at the interacting tips (inner tips) of surfaces than at the outer tips. The rate of change of the absolute values was found to be lower for smaller values of surface elasticity parameter. Additionally, the absolute values of the same factors at the tips of inclined surfaces were smaller for smaller values of surface tension, while those at the tips of horizontal surfaces were larger. Under the same far-field loading, the Mode II stress intensity factor was zero at the tips of inclined surfaces, in the case of vanishing surface tension, and had non-zero value in the case of non-zero surface tension. Interestingly, the latter factor was zero at the tips of the horizontal surface in both cases.

Finally, we presented the results that illustrated the influences of the two types of applied far-field loads on the relative Von-Mises stresses for the three configurations used in the numerical studies.

The theoretical framework presented here allows for natural extensions to problems involving materials reinforced with thin, stiff, and prestressed inhomogeneities/layers of arbitrary shapes. This will be a subject of our

future work in which we also plan to extend the presented approach to allow for evaluation of the effective properties of such materials. The results of this paper can be used as benchmarks for proposed extensions as well as for future investigators.

# Acknowledgements

The authors gratefully acknowledge the support from the National Science Foundation, United States, award number NSF CMMI - 2112894. The first author gratefully acknowledges the Charles Fairhurst Fellowship in Earth Resources Engineering, University of Minnesota. We would also like to thank Prof. Alexander Movchan for the fruitful discussions related to the topic of this paper.

# Appendix A. Some details of derivations Eqs. 58-60

The governing equations of plane strain problems in complex variables are given by the following Kolosov-Muskhelishvili formulae [45]:

$$\sigma_{11} + \sigma_{22} = 4 \operatorname{Re}[\phi'(z)],$$

$$\sigma_{22} - \sigma_{11} + 2i\sigma_{12} = 2 \left[ \overline{z} \phi''(z) + \psi'(z) \right],$$
(A.1)

where  $\phi(z)$  and  $\psi(z)$  are the holomorphic functions. It can be shown, see [42], that those functions for our case of continuity of displacements and jump in tractions can be represented as follows:

$$\phi'(z) = \frac{1}{2\pi i(1+\kappa)} \int_{L} \frac{\Delta \sigma}{(\tau-z)} d\tau,$$

$$\phi''(z) = \frac{1}{2\pi i(1+\kappa)} \int_{L} \frac{\Delta \sigma}{(\tau-z)^{2}} d\tau,$$

$$(A.2)$$

$$\psi'(z) = \frac{1}{2\pi i(1+\kappa)} \left[ \kappa \int_{L} \frac{\overline{\Delta \sigma}}{(\tau-z)} d\tau - \int_{L} \frac{\overline{\tau} \Delta \sigma}{(\tau-z)^{2}} d\tau \right].$$

Using the appropriate dimensionlization, resulting expressions for the stresses contain four integrals, see Eqns. A.3-A.6. Here, we present the

asymptotic expansions at the point  $\tilde{z} = z/a$  for the stresses in the vicinity of the tip  $\tilde{\tau} = -1$  in the form  $\tilde{z} = -1 + \tilde{r} \exp{(i\theta)}, -\pi \le \theta < \pi$ . The corresponding expressions for the tip  $\tilde{\tau} = 1$  can be found in [34], [35].

The leading terms in the near-tip expansions of those integrals are evaluated using the results on the behavior of the singular integrals near the tips reported in Chapter 4 of Ref. [46] and on page 21 of Ref. [47] as

Integral 1:

$$\int_{-1}^{1} \frac{\Delta \widetilde{\sigma} \, d\widetilde{\tau}}{(\widetilde{\tau} - \widetilde{z})} \approx -\frac{\pi i}{\sqrt{2}} \sigma^*(-1) \frac{1}{\sqrt{1 + \widetilde{z}}} = -\frac{\pi i}{\sqrt{2} \, \widetilde{r}} [\sigma^*(-1)] \exp(-i\theta/2) , \quad (A.3)$$

Integral 2:

$$\int_{-1}^{1} \frac{\overline{\Delta \widetilde{\sigma}} \, \overline{d\widetilde{\tau}}}{\overline{\widetilde{\tau}} - \overline{\widetilde{z}}} \approx \frac{\pi i}{\sqrt{2}} \overline{\sigma^*(-1)} \frac{1}{\sqrt{1 + \overline{\widetilde{z}}}} = \frac{\pi i}{\sqrt{2} \, \widetilde{r}} [\overline{\sigma^*(-1)}] \exp(i\theta/2) , \qquad (A.4)$$

Integral 3:

$$\int_{-1}^{1} \frac{\Delta \widetilde{\sigma} \, d\widetilde{\tau}}{\overline{\overline{\tau}} - \overline{\overline{z}}} \approx \frac{\pi i}{\sqrt{2}} \sigma^{*}(-1) \frac{1}{\sqrt{1 + \overline{\overline{z}}}} = \frac{\pi i}{\sqrt{2} \, \widetilde{r}} [\sigma^{*}(-1)] \exp(i\theta/2) , \qquad (A.5)$$

Integral 4:

$$\int_{-1}^{1} \frac{\overline{\Delta \widetilde{\sigma}} (\widetilde{\tau} - \widetilde{z}) \, \overline{d\widetilde{\tau}}}{(\overline{\widetilde{\tau}} - \overline{\widetilde{z}})^{2}} \approx \frac{\pi i}{2\sqrt{2}} \overline{\sigma^{*}(-1)} \left[ 1 + \frac{1 + \widetilde{z}}{1 + \overline{\widetilde{z}}} \right] \frac{1}{\sqrt{1 + \overline{\widetilde{z}}}}$$

$$= \frac{\pi i}{2\sqrt{2} \, \widetilde{r}} [\overline{\sigma^{*}(-1)}] \exp(i\theta/2) (1 + \exp(2i\theta)) , \tag{A.6}$$

where

$$\Delta \widetilde{\sigma} = \frac{\sigma^*(\widetilde{\tau})}{\sqrt{1 - (\widetilde{\tau})^2}} \,. \tag{A.7}$$

After substituting the expressions from Eqs. A.3 to A.6 into the dimensionalized form of Eq. A.1 and performing some algebra, we can obtain the expressions given by Eq. 58 through Eq. 60.

#### References

- [1] W.T. Koiter. On the diffusion of load from a stiffener into a sheet. Q. J. Mech. Appl. Math., 8(2):164–178, 1955.
- [2] D. Caillerie and J.C. Nedelec. The effect of a thin inclusion of high rigidity in an elastic body. *Math. Methods Appl. Sci.*, 2:251–270, 1980.
- [3] Z.Y. Wang, H.T. Zhang, and Y.T. Chou. Characteristics of the elastic field of a rigid line inhomogeneity. *J. Appl. Mech.*, 52:818–822, 1985.
- [4] R. Ballarini. A rigid line inclusion at a bimaterial interface. *Eng. Fract. Mech.*, 37(1):1–5, 1990.
- [5] X. Markenscoff. On the Dundurs correspondence between cavities and rigid inclusions. J. Appl. Mech., 60:260–264, 1993.
- [6] C. Atkinson. Some ribbon-like inclusion problems. Int. J. Eng. Sci., 11:243–266, 1973.
- [7] Y.K. Cheung and Y.Z. Chen. Multiple rigid line problems in an infinite plate. *Eng. Fract. Mech.*, 34(2):379–391, 1989.
- [8] K.C. Wu. Line inclusions at anisotropic bimaterial interface. *Mech. Mater.*, 10(3):173–182, 1990.
- [9] C.P. Jiang and Y.K. Cheung. Antiplane problems of collinear rigid line inclusions in dissimilar media. *Eng. Fract. Mech.*, 52(5):907–916, 1995.
- [10] C.Y. Dong, S.H. Lo, and Y.K. Cheung. Interaction between cracks and rigid-line inclusions by an integral equation approach. *Comput. Mech.*, 31(3):238–252, 2003.
- [11] F. D. Corso, D. Bigoni, and M. Gei. The stress concentration near a rigid line inclusion in a prestressed, elastic material. part i.: Full-field solution and asymptotics. *J Mech Phys Solids*, 56(3):815–838, 2008.
- [12] D. Bigoni, F. D. Corso, and M. Gei. The stress concentration near a rigid line inclusion in a prestressed, elastic material. part ii.:: Implications on shear band nucleation, growth and energy release rate. *J Mech Phys Solids*, 56:839–857, 2008.

- [13] D. Misseroni, F. D. Corso, S. Shahzad, and D. Bigoni. Stress concentration near stiff inclusions: Validation of rigid inclusion model and boundary layers by means of photoelasticity. *Eng. Fract. Mech.*, 121-122:87–97, 2014.
- [14] P. Pingle, J. Sherwood, and L. Gorbatikh. Properties of rigid-line inclusions as building blocks of naturally occurring composites. *Mech. Mater.*, 68(10):2267–2272, 2008.
- [15] T.M. Jobin, M. Ramji, and S.N. Khaderi. Numerical evaluation of the interaction of rigid line inclusions using strain intensity factors. *Inter*national Journal of Mechanical Sciences, 153:10–20, 2019.
- [16] Z. Hashin. Thermoelastic properties of particulate composites with imperfect interface. J Mech Phys Solids, 39(6):745–762, 1991.
- [17] A. Klarbring. Derivation of a model of adhesively bonded joints by the asymptotic expansion method. *Int. J. Eng. Sci.*, 29(4):493–512, 1991.
- [18] P. Bövik. On the modelling of thin interface layers in elastic and acoustic scattering problems. Q. J. Mech. Appl. Math., 47(1):17–42, 1994.
- [19] D. Bigoni, S.K. Serkov, M. Valentini, and A.B. Movchan. Asymptotic models of dilute composites with imperfectly bonded inclusions. *Int J Solids Struct*, 35(24):3239–3258, 1998.
- [20] Y. Benveniste and T. Miloh. Imperfect soft and stiff interfaces in two-dimensional elasticity. *Mech. Mater.*, 33(6):309–323, 2001.
- [21] M. Serpilli, R. Rizzoni, F. Lebon, and S. Dumont. An asymptotic derivation of a general imperfect interface law for linear multiphysics composites. *Int J Solids Struct*, 180:97–107, 2019.
- [22] S. Baranova, S.G. Mogilevskaya, T.H. Nguyen, and D. Schillinger. Higher-order imperfect interface modeling via complex variables based asymptotic analysis. *Int. J. Eng. Sci.*, 157:103399, 2020.
- [23] S. Firooz, P. Steinmann, and A. Javili. Homogenization of composites with extended general interfaces: comprehensive review and unified modeling. *Applied Mechanics Reviews*, 73(4):040802, 2021.

- [24] S. Baranova and S.G. Mogilevskaya. On the Bövik–Benveniste methodology and related approaches for modelling thin layers. *Philos. Trans. Royal Soc. A*, 380(2231):20210420, 2022.
- [25] D.V. Grilitskii and G.T. Sulim. Periodic problem for an elastic plane with thin-walled inclusions. *J. Appl. Math. Mech.*, 39(3):494–503, 1975.
- [26] D.V. Grilitskii, A.A. Evtushenko, and G.T. Sulim. Stress distribution in a strip with a thin elastic inclusion. J. Appl. Math. Mech., 43(3):582– 589, 1979.
- [27] G.T. Sulim. Stress concentration next to thin-walled linear inclusions. Sov. Appl. Mech., 17:1011–1017, 1981.
- [28] B.L. Wang and J.E. Li. Multiple elastic or rigid line inclusions in a multilayered orthotropic solid. *Mech. Mater.*, 169(3):104306, 2022.
- [29] M.E. Gurtin and A.I. Murdoch. A continuum theory of elastic material surfaces. *Arch. Ration. Mech. Anal.*, 57:291–323, 1975.
- [30] M.E. Gurtin and A.I. Murdoch. Surface stress in solids. *Int. J. Solids Struct.*, 14:431–440, 1978.
- [31] D.J. Steigmann and R.W. Ogden. Plain deformations of elastic solids with intrinsic boundary elasticity. *Proc. R. Soc. London A*, 453:853–877, 1997.
- [32] D.J. Steigmann and R.W. Ogden. Elastic surface-substrate interactions. *Proc. R. Soc. A*, 455(1982):437–474, 1999.
- [33] S. Baranova, S.G. Mogilevskaya, V. Mantič, and S. Jiménez-Alfaro. Analysis of the antiplane problem with an embedded zero thickness layer described by the Gurtin-Murdoch model. *J. Elast.*, 140:171–195, 2020.
- [34] S.G. Mogilevskaya, A.Y. Zemlyanova, and V. Mantič. The use of the Gurtin-Murdoch theory for modeling mechanical processes in composites with two-dimensional reinforcements. *Compos. Sci. Technol.*, 210:108751, 2021.
- [35] A. Y. Zemlyanova, S. G. Mogilevskaya, and D. Schillinger. Numerical solution of the two-dimensional Steigmann-Ogden model of material surface with a boundary. *Physica D*, 443(133531), 2023.

- [36] A. Y. Zemlyanova and L. M. White. An axisymmetric problem for a patch loaded material surface attached to the boundary of an elastic semi-space. SIAM Journal on Applied Mathematics, 83(2):603–624, 2023.
- [37] A. Y. Zemlyanova. A problem for a material surface attached to the boundary of an elastic semi-plane. *Mathematics and Mechanics of Solids*, 29(2):303–326, 2024.
- [38] S.G. Mogilevskaya, A.Y. Zemlyanova, and V.I. Kushch. Fiber- and particle-reinforced composite materials with the Gurtin–Murdoch and Steigmann–Ogden surface energy endowed interfaces. *Appl. Mech. Rev.*, 73(5), 2021.
- [39] V.D. Kupradze. Potential Methods in the Theory of Elasticity. Israel Program for Scientific Translations, Jerusalem (Translation of Russian edition. 1963. Gos. Izdat. Fiz-Mat Lit, Moscow), 1965.
- [40] S.G. Mogilevskaya. Lost in translation: Crack problems in different languages. *Int. J. Solids Struct.*, 51:4492–4503, 2014.
- [41] S.G. Mogilevskaya and A.M. Linkov. Complex fundamental solutions and complex variables boundary element method in elasticity. *Comput. Mech.*, 22:88–92, 1998.
- [42] A.M. Linkov. Boundary Integral Equations in Elasticity Theory. Kluwer Academic Publishers, Dordrecht, Netherlands, 2002.
- [43] A.M. Linkov and S.G. Mogilevskaya. Complex hypersingular BEM in plane elasticity problems. *In: Sladek, V., Sladek, J. (Eds.), Singular Integrals in Boundary Element Method, Chapter 9. Computational Mechanics Publication*, pages 299–364, 1998.
- [44] D.G. Papageorgiou, I.A. Kinloch, and R.J. Young. Mechanical properties of graphene and graphene-based nanocomposites. *Prog. Mater. Sci.*, 90:75–127, 2017.
- [45] N.I. Muskhelishvili. Some Basic Problems of the Mathematical Theory of Elasticity. Noordhoff, 1963.

- [46] N.I. Muskhelishvili. Singular integral equations. Dover Publication, 2nd edition edition, 1992.
- [47] M.P. Savruk. Two-Dimensional Problems of Elasticity for Bodies with Cracks. Naukova Dumka [in Russian], 1981.